NASA TECHNICAL NOTE

NASA TN D-3447

NASA TN D-3447

MEASURED AND CALCULATED FLOW CONDITIONS ON THE FORWARD FUSELAGE OF THE X-15 AIRPLANE AND MODEL AT MACH NUMBERS FROM 3.0 TO 8.0

by Murray Palitz

Flight Research Center
Edwards, Calif.

NATIONAL AERONAUTICS AND SPACE ADMINISTRATION • WASHINGTON, D. C. • JUNE 1966

NASA TN D-3447

MEASURED AND CALCULATED FLOW CONDITIONS ON THE FORWARD FUSELAGE OF THE X-15 AIRPLANE AND MODEL AT MACH NUMBERS FROM 3.0 TO 8.0

By Murray Palitz

Flight Research Center
Edwards, Calif.

NATIONAL AERONAUTICS AND SPACE ADMINISTRATION

For sale by the Clearinghouse for Federal Scientific and Technical Information
Springfield, Virginia 22151 – Price $2.00

MEASURED AND CALCULATED FLOW CONDITIONS ON THE FORWARD FUSELAGE OF THE X-15 AIRPLANE AND MODEL AT MACH NUMBERS FROM 3.0 TO 8.0

By Murray Palitz
Flight Research Center

SUMMARY

Impact-pressure and surface static-pressure measurements obtained from the X-15 configuration in flight and wind-tunnel tests are presented and compared with calculated results. Flight and wind-tunnel data are presented for angles of attack of 0° to 18° and 0° to 20°, respectively, and free-stream Mach numbers from 0.8 to 5.5 and 2.3 to 8.0, respectively.

In regions near the body, the impact-pressure and surface static-pressure measurements from flight and wind tunnel at angles of attack were used to derive local Mach numbers. The results are compared with values obtained by using methods developed from simple flow models. The flight and wind-tunnel Mach number profiles for a detached-shock (spherical, or blunt, nose) configuration at zero angle of attack agree with numerical solutions of Moeckel-Love and Inouye-Lomax. Wind-tunnel impact and surface static pressures for an attached-shock (conical, or pointed, nose) configuration (free-stream Mach numbers of 4.7 to 8.0) agree with the method-of-characteristics solution for zero angle of attack.

INTRODUCTION

As Mach number increases, large flow gradients are induced near the surface of blunt bodies by the detached and rapidly attenuating shock wave. Typical wind-tunnel investigations of this effect on two- and three-dimensional bodies are reported in references 1 to 6. This development affects the characteristics of the boundary layer, particularly the heat transfer.

Early analyses of X-15 flight heat-transfer data (refs. 7 to 9) were based on calculated values of the local-flow conditions. The resultant differences between measured and predicted heat transfer were thought to be partially due to an incomplete knowledge of the local fluid properties. Subsequently, a flight investigation was made to determine the extent and character of the local flow on the X-15 airplane in order to aid in the interpretation of the measured heat-transfer data. The results of the flow-field investigation on the forebody of the X-15 are presented and analyzed in this paper. Flight data

are shown for the Mach number range of 0.8 to 5.5 at Reynolds numbers from 0.5 to 2.0×10^6 per foot. Relevant full-scale static-pressure data obtained from previous X-15 flights are reported in reference 10. Some local Mach number and surface static-pressure results obtained from the wedge-shaped upper vertical fin on the X-15 were reported in reference 11 for both a cylindrical and a sharp-leading-edge configuration.

Wind-tunnel studies of the local-flow characteristics on an X-15 model were reported in references 12 and 13. These results and results from more recent wind-tunnel investigations are compared herein with the full-scale flight data. In addition, calculations obtained by using several simplified analytical flow models are compared with the results of this study.

SYMBOLS

C_p pressure coefficient, $\frac{(p - p_\infty)}{0.7 p_\infty M_\infty^2}$

k Newtonian constant, $\frac{p_{i_\infty} - p_\infty}{0.7 p_\infty M_\infty^2}$

l airplane length (594), inches

M Mach number

p static pressure

p_i impact pressure, total pressure behind normal shock

p_s surface static pressure

N_{Re} Reynolds number, $\frac{ux}{\nu}$

u velocity

x distance measured along the centerline of the airplane from the ball-nose stagnation point, inches

y distance measured from the surface perpendicular to centerline for model tests, inches

y' distance measured perpendicular to surface for flight tests (fig. 4), inches

α angle of attack, degrees

δ surface angle with respect to free-stream flow

θ surface inclination in the direction of the forward stagnation region, with respect to body centerline (see figs. 2 and 4)

ν dynamic viscosity

φ circumferential angle (fig. 4)

Subscripts:

l local conditions

∞ free stream

VEHICLE DESCRIPTION

Airplane

A three-view drawing of the X-15 airplane is shown in figure 1. The forward fuselage consists of a spherical flow-direction sensor (ref. 14) faired into an ogive through two truncated cones (fig. 2(a)). The ogive is generated from the arc of a 700-inch-radius circle, whose center is at $x = 188$ inches and 672 inches from the centerline. The ogive forebody is tangent to the cylindrical aft region at $x = 188$ inches.

Further details on the X-15 configuration are presented in reference 10.

Model

A 1/15-scale model of the X-15 was used in the wind-tunnel tests considered in this paper over the Mach number range from 2.3 to 8.0. In addition to the spherical (blunt) nose, a conical 15° half-angle cone was used to provide an attached-shock (pointed) configuration. The blunt- and the pointed-model nose are compared in figure 2(b). Surface-pressure orifices along the lower centerline of the model were used to obtain data for these tests.

Details of the model geometry and pressure-orifice locations are presented in references 12 and 13.

INSTRUMENTATION

Flight

Pitot rakes were installed at several accessible locations on the airplane fuselage, parallel to the local ray originating at the forward stagnation point, and perpendicular to the surface. A photograph of a typical rake installation is shown in figure 3. Location and dimensions of the rakes and

local surface geometry are presented in figure 4. The rakes were constructed from Inconel tubing, bent to shape and sandwiched between Inconel plates. Static-pressure orifices, flush with the surface, were located within 2 inches of the base of the rakes. Aerodynamic design information for the rakes was obtained from wind-tunnel investigations such as those of references 15 to 19.

Flight measurements were obtained from standard NACA aneroid-type manometers or electrical transducers in combination with 36-channel oscillographs. Both systems reflected a ray of light continuously on film. A typical aneroid cell is shown in figure 5. Both systems gave pressure readings with an accuracy of about 1 percent of the pressure range of the instrumentation. It is estimated that this percentage error resulted in a 2-percent accuracy for the impact-pressure measurements, whereas the accuracy of local static-pressure measurements varied with pressure level from 2 percent at $x = 20$ inches to 10 percent at $x = 188$ inches.

Angles of attack and sideslip and free-stream impact pressures were obtained from the flow-direction sensor (ref. 14). A timer synchronized all onboard records. Altitude and velocity were obtained from radar tracking, and free-stream properties were derived from radiosonde measurements through the use of techniques discussed in reference 20.

Wind Tunnel

Model tests to obtain impact-pressure and surface static-pressure data were conducted at the Arnold Engineering Development Center (AEDC) and the NASA Langley Research Center.

The impact-pressure surveys were made at several stations along the lower centerline of the model. The surveys were made perpendicular to the centerline of the model, from the surface of the shock, by a traversing probe. The tests at $M_\infty = 4.7$ were made in the Langley 4- by 4-foot Unitary Plan Wind Tunnel and at $M_\infty = 8.0$ in the AEDC von Kármán Gas Dynamics Facility Tunnel B.

The surface static pressures were obtained at Langley for $M_\infty = 2.3$, 2.88, and 4.65, and at AEDC for $M_\infty = 4.0$, 5.0, 6.0, and 8.0.

Detailed information on the wind-tunnel recording instrumentation is included in references 21 to 23.

PRESENTATION OF RESULTS

All pressure data presented are nondimensionalized with respect to free-stream conditions. Static pressure is presented as a ratio of local static pressure p_l to free-stream static pressure p_∞, and measured impact pressure as a ratio of local impact pressure p_{i_l} to free-stream impact pressure p_{i_∞}.

These quantities are the total pressures behind the normal shock ahead of each probe in the flow field p_{i_l} and free stream p_{i_∞}. This approach simplified correlation between flight, wind tunnel, and theory.

The coordinates of the wind-tunnel-model test results are presented in terms of full scale. Local Mach numbers were obtained by using the Rayleigh pitot-tube formula based on the surface static pressures and the measured impact pressure through the flow field. Flight data, comparative wind-tunnel data, and theoretical results are presented in figures 6 to 21. For convenience, flight-test and wind-tunnel-test conditions are presented in the following tables:

FLIGHT TEST CONDITIONS[a]

Parameter	M_∞	α, deg	x, in.	Figure
p_s/p_∞	$2.1 < M_\infty < 5.5$	0	20, 52, 74, 138, 188	6
p_s/p_∞	4.7	0, 5, 10, 20	20, 52, 74, 138, 188	7(a)
p_{i_l}/p_{i_∞}	$3.2 < M_\infty < 5.1$ $0.8 < M_\infty < 5.4$	0 0	20 74	8(a) 8(b)
p_{i_l}/p_{i_∞}	3.0	0, 5, 10	20	11(a)
p_{i_l}/p_{i_∞}	4.0	0, 4, 10, 12	20	11(b)
p_{i_l}/p_{i_∞}	4.7	0, 5, 11, 17	20	11(c)
p_{i_l}/p_{i_∞}	5.4	0, 5, 11, 17	20	11(d)

[a]Flight Reynolds number varied from 0.5 to 2.0 x 10^6 per foot.

WIND-TUNNEL-TEST CONDITIONS

Impact pressures

M_∞	α, deg	Nose configuration[b] x, inches					Unpublished data source	N_{Re} per foot	Figure
		15	27	45	74	192			
4.7	0		B,P		B,P	B,P	Langley 4- by 4-foot Unitary Plan tunnel	3.2 x 10^6	9(a), 9(b), 13(a) to 13(c)
4.7	5		B		B	B,P	↓	↓	13(a) to 13(c)
4.7	10		B		B	B,P	↓	↓	13(a) to 13(c)
4.7	20				B	B	↓	↓	13(a) to 13(c)
8.0	0	B,P	B,P	B,P	B,P	B	AEDC von Kármán Gas Dynamics Facility Tunnel B	3.4 x 10^6	10(a) to 10(d), 14(a) to 14(d)
8.0	5	B		P	P	B	↓	↓	14(a) to 14(d)
8.0	10			B,P	B,P	B	↓	↓	14(a) to 14(d)
8.0	15					B	↓	↓	14(a) to 14(d)
8.0	20				B,P	B	↓	↓	14(a) to 14(d)

[b]P denotes pointed (conical) nose; B, blunt (spherical) nose.

WIND-TUNNEL-TEST CONDITIONS

Surface static pressures

M_∞	α, deg	Nose configuration[a]	Data source	N_{Re} per foot	Figure
2.3	0	B	Langley 4- by 4-foot Unitary Plan tunnel (ref. 24)	2.7×10^6	6
2.9	0	B	Langley 4- by 4-foot Unitary Plan tunnel (ref. 24)	5.2×10^6	6
4.0	0	B	AEDC von Kármán Gas Dynamics Facility Tunnel A	3.4×10^6	6
4.7	0	B,P	Langley 4- by 4-foot Unitary Plan tunnel	3.2×10^6	7(a)
4.7	5	B,P	↓	↓	7(a)
4.7	10	B,P	↓	↓	7(a)
4.7	20	B	↓	↓	7(a)
5.0	0	B	AEDC von Kármán Gas Dynamics Facility Tunnel A	3.4×10^6	6
6.0	0	B	↓	↓	6
8.0	0	B,P	AEDC von Kármán Gas Dynamics Facility Tunnel B	↓	7(b)
8.0	5	B,P	↓	↓	7(b)
8.0	10	B,P	↓	↓	7(b)
8.0	15	B,P	↓	↓	7(b)
8.0	20	B,P	↓	↓	7(b)

[a]P denotes pointed (conical) nose; B, blunt (spherical) nose.

DISCUSSION OF RESULTS

Surface Static Pressures

Flight measurements, in the form of normalized surface static pressures, are shown in figure 6 as a function of free-stream Mach number for several fuselage stations at zero angle of attack. The figure also includes wind-tunnel data obtained through interpolation, and theoretical results from the detached-shock solution of Inouye-Lomax. Flight, wind tunnel, and predicted surface static pressures agree at all stations except x = 188 inches. The deviation of flight data from wind tunnel and theory at this location is believed to be caused by the flow-interference effects of an antenna that extends 5 inches from the surface (frontal diameter approximately 0.7 inch) and is located 36 inches forward of the orifice and a flush-mounted antenna (recessed approximately 0.06 inch) located approximately 3 inches forward of the orifice.

Surface static-pressure ratios obtained from flight and wind-tunnel tests are shown in figures 7(a) and 7(b). The data are presented as a function of

longitudinal distance along the lower centerline of the X-15 over the angle-of-attack range from 0° to 20° and are compared with results obtained from the theoretical solutions for the blunt- and pointed-nose configurations and from several simplified flow models, as discussed in the appendix.

The Inouye-Lomax prediction of the normalized surface pressures at zero angle of attack for the blunt-nose configuration indicates an overexpansion of the flow around the shoulder at the sphere-ogive junction. This expansion results in surface static pressures lower than predicted by the pointed (attached shock) method of characteristics. The wind-tunnel data obtained at $\frac{x}{l} = 0.03$ for a blunt- and a pointed-nose configuration also indicate that this expansion takes place and, furthermore, that the effect of nose configuration in this region extends to at least $\alpha = 10°$ at $M_\infty = 4.7$ and 8.0. The effect of nose configuration on the normalized surface pressures is small for $\frac{x}{l} > 0.08$ over the angle-of-attack and Mach range considered.

The effect of angle of attack for the ogive section of the model (between $\frac{x}{l} = 0.08$ and 0.33) is most closely predicted by the modified Newtonian theory at $M_\infty = 4.7$ and the conical-shock-expansion method at $M_\infty = 8.0$ for angles of attack of 10° and above.

Impact Pressures

Zero angle of attack.— Impact-pressure measurements obtained in flight at $x = 20$ inches on the lower centerline of the X-15 are shown in figure 8(a). The data are plotted as a function of free-stream Mach number and are compared with results obtained from the Inouye-Lomax solution. The flight data up to 1.25 inches from the surface are lower than the calculated results. This is attributed to a disturbance originating off the lip of the spherical nose-cone junction. The data above 1.25 inches show better agreement, both in level and in trend, with the calculated results.

Figure 8(b) presents impact-pressure ratios obtained at $x = 74$ inches at two circumferential locations. The data are compared with wind-tunnel measurements and results from the Inouye-Lomax solution. These impact-pressure ratios, at zero angle of attack for both flight and wind tunnel, show good agreement with the theory at this station. There is no indication of effects from circumferential location.

Impact-pressure ratios plotted as a function of distance from the surface are presented in figures 9(a) and 9(b) and 10(a) to 10(d) for the X-15 wind-tunnel model with a pointed- and a blunt-nose configuration. These data surveyed from the lower centerline of the 1/15-scale wind-tunnel model are conpared with results obtained from the theoretical solutions for blunt- and pointed-nose configurations.

The normalized impact pressures show a distinct effect of nose configuration on the local flow. For example, a change from a detached- to an attached-shock configuration (blunt to pointed) results in a reduction in both the variation of the impact-pressure curve from the surface to the shock and in the vertical location of the shock wave. It also results in an increase in the level of the impact-pressure curves for values of x less than 74 inches. The agreement in level and trend of the impact pressures at 74 inches and beyond (fig. 13(c)), for heights greater than 2 inches from the surface, results from the rapid attenuation of the detached shock wave to the general shape and strength of that associated with the attached shock. The initial shear-layer development (caused by the rapidly changing shock-wave shape in the stagnation region) is related to the increase in cross-sectional area with increasing longitudinal distance. This increase in cross-sectional area results in a greater wetted area on the ogival forebody. Conservation of mass and momentum within the shear layer in combination with the additional wetted area has the effect of decreasing the height of the shearing region as the flow progresses over the forebody, thus limiting configuration effects at $x = 74$ inches to approximately 2 inches from the surface.

The Inouye-Lomax solution predicts the level, shape, and shock location of the inviscid shear layer but overestimates the impact pressure at $x = 27$ inches. This theory adequately predicts the levels of the shearing layer at the other locations.

Effect of angle of attack.— Normalized impact-pressure measurements obtained in flight at $x = 20$ inches are presented in figures 11(a) to 11(d) at four representative free-stream Mach numbers for angles of attack up to 17°. The data are shown as a function of distance y' from the surface. The normalized impact pressures at angles of attack above 11° exhibit a sharp pressure discontinuity. This pressure jump is characteristic of the effect of an embedded shock in the flow field. The development of the shock system in the forward area of the flight vehicle is similar to the shock system in the schlieren photographs of figures 12(a) to 12(d). The configuration photographed is that of a preliminary design flow-direction sensor closely resembling the X-15 flight instrument in general shape. The divergences in shape between the model and flight instrument do not affect the qualitative picture of the internal shock development. This development, over the angle-of-attack range considered, of the bow shock and the embedded shock off the lip at the junction of the sphere and cone can be seen in the figure.

The normalized impact-pressure data obtained from the model surveys at angles of attack up to 20° for the pointed- and the blunt-nose configuration are presented as a function of height y from the surface in figures 13(a) to 13(c) and 14(a) to 14(d). The level of the impact pressure increases with angle of attack, whereas the vertical extent of the flow field is reduced. The effect of nose configuration is not significant for $x = 45$ inches (fig. 14(b)) or 74 inches (fig. 14(c)) for angles of attack above 5°. The normalized impact pressures at $x = 192$ inches are presented in figures 13(c) and 14(d). The measurements agree with results obtained from the Inouye-Lomax solution at zero angle of attack and show the same trends as the other longitudinal stations with increasing angle of attack.

Mach Number Profiles

Zero angle of attack.— Mach number distributions through the flow field obtained from the Inouye-Lomax solution are presented at several selected stations along the sphere-ogive-cylinder (X-15 shape) in figures 15(a) and 15(b). The distributions are shown for $M_\infty = 4.7$ and 8.0 as functions of height from the surface. The Mach number level increases with longitudinal distance. This increase in local Mach number results from the expansion of the flow around the ogive forebody and reaches a maximum behind the ogive-cylinder junction (x = 192 in.), indicating a slight overexpansion of the flow in this area. The flow recovers to a relatively constant value at x = 350 inches.

The theoretical calculations from the Inouye-Lomax solution for the local static-pressure variation through the flow field are presented in figures 16(a) and 16(b). The level of the normalized static pressures decreases with increasing distance back from the nose region. This results from the longitudinal expansion of the flow around the ogive forebody. The static-pressure variation through the flow field in the region between x = 15 inches and x = 27 inches is approximately constant up to 3 inches from the surface in both the variation through the flow field and longitudinal gradient on the surface. Therefore, the surface static pressure was assumed to be constant through the flow field at x = 20 inches for the analysis of the flight data, even though the impact pressures near the surface showed the effects of a shock off the lip of the flow-direction sensor.

The local Mach numbers, derived from the impact- and surface static-pressure measurements, are presented from flight in figures 17(a) and 17(b) and from wind-tunnel tests in figure 18. These values are compared with results obtained from the Inouye-Lomax and the Moeckel-Love methods. Both methods satisfactorily predict the local Mach number level near the surface. The Moeckel-Love method, which is relatively easy to use, can predict the local Mach number in areas where surface static-pressure values are known and where relatively small variations in static-pressure level above the surface exist.

Effect of angle of attack.— Local Mach number data derived from flight impact and surface static pressures obtained at x = 20 inches are presented in figures 19(a) to 19(c). The data are shown as a function of angle of attack and for heights within 1.0 inch of the surface; the effect of shock interaction beyond this height is unknown. The data are presented as a function of angle of attack to emphasize the relatively small variation in Mach number at this location over the angle-of-attack range shown. This result is believed to be due to the complex nature of the flow field forward of this area--a region of shock interaction and flow expansion behind the sphere—cone junction.

The local Mach numbers derived from wind-tunnel impact-pressure data, assuming a constant static pressure from the surface, are presented in figures 20(a) to 20(c) and 21(a) to 21(c). The data are shown as a function of distance from the surface for angles of attack of 0°, 10°, and 20°. These values are compared with predictions obtained by using several simplified flow models. As can be seen in the figures, predicted values obtained from Moeckel-Love and the more exact Inouye-Lomax numerical method show good agreement up to at least 1 inch from the surface back to 74 inches from the nose for $\alpha = 0°$.

The deviation between the Inouye-Lomax Mach number values and the measurements in figure 21(a) results from the assumption of a constant static pressure through the flow field used in conjunction with the measured impact pressures to obtain the experimental Mach number data. This assumption is valid at $M_\infty = 4.7$ (fig. 16(a)) where little deviation exists between the surface and local static-pressure values through the flow field up to 4 inches. Greater deviation between the local and surface static-pressure values exists at $M_\infty = 8.0$ (fig. 16(b)), particularly above 1.0 inch from the surface.

Extending the Moeckel-Love method to angles of attack results in better agreement with the measured data at $M_\infty = 4.7$ (fig. 20) than at $M_\infty = 8.0$ (fig. 21), although in both instances neither the measured gradients nor the levels are satisfactorily predicted. This result is not unexpected, since the method does not take into account the expansion of the flow around the body or a change in the shock shape at angle of attack. Of the approximate flow models considered, the tangent-cone prediction appears to offer the closest approximation to the local Mach number over the Mach number range considered for angles of attack greater than zero at the outer edge of the shear layer.

CONCLUSIONS

Comparison of surface static pressures, impact-pressure profiles, and Mach number profiles from the X-15 configuration in flight, in the wind tunnel, and calculated from theory provided the following results:

1. Normalized surface static pressures obtained from the lower centerline of the X-15 forebody in flight and from the 1/15-scale wind-tunnel model agreed for locations where geometric similarity was maintained. This comparison covered a free-stream Mach number range from about 2.1 to 5.5 for zero angle of attack and angles of attack up to 20° for a free-stream Mach number of 4.7.

2. The numerical solution of Inouye-Lomax closely predicted the experimentally determined static pressures for the lower centerline of the X-15 configuration for free-stream Mach numbers of 4 and above at zero angle of attack. The effects of angle of attack were predicted most closely by the modified Newtonian method for a free-stream Mach number of 4.7. At a free-stream Mach number of 8.0 and angles of attack of 10° and above, the conical-shock-expansion method provided the best prediction.

3. The Inouye-Lomax method adequately predicted the measured full-scale and wind-tunnel impact-pressure values through the shear layer at free-stream Mach numbers of 4 and above at zero angle of attack.

4. The Moeckel-Love method agreed with the more exact numerical solutions of Inouye-Lomax at locations along the forebody where constant static pressure can be assumed through the flow field.

Flight Research Center,
National Aeronautics and Space Administration,
Edwards, Calif., February 11, 1966.

APPENDIX

CALCULATION METHODS

Predicted normalized impact pressures, static pressures, and local Mach numbers were obtained by using the method of characteristics and other numeric solutions for the axisymmetric body configuration at zero angle of attack and from methods developed from simple flow models for angles of attack. The methods used are briefly discussed in the following sections.

Newtonian (Surface Pressures)

This method is discussed in reference 25. The basic Newtonian equation may be presented as

$$C_p = k \sin^2\delta$$

where C_p is the pressure coefficient, δ is the local surface deflection (surface angle with respect to the free-stream direction of flow), and k is a constant. The above relationship has been found to give reasonably good predictions of pressure distribution on bodies if the proper value of k is determined. The constant k was assumed equal to the pressure coefficient at the stagnation point for the cases considered, which resulted in the following modified Newtonian equation

$$\frac{p_s}{p_\infty} = \left(\frac{p_{i_\infty}}{p_\infty} - 1\right) \sin^2\delta + 1$$

Tangent Cone

It is assumed that the local static pressure is equivalent to the pressure on a cone with a semi-vertex angle equal to the angle between the tangent to the surface and the direction of the flow (ref. 26). Chart 7 of reference 27 may be used to obtain this value. It should be noted that this method assumes a total-pressure variation along the fuselage.

Conical-Shock Expansion

To apply this method for a blunt body, an initial cone angle is assumed (ref. 26). The surface Mach number on this cone is determined, and flow quantities downstream of the vertex can then be obtained by applying the Prandtl-Meyer expansion equation or using the tabulated values in reference 27. This method assumes a constant total pressure along the fuselage.

Method of Characteristics

Theoretical predictions for the pointed-nose (attached shock) configuration were obtained by using the method-of-characteristics solution for the X-15 shape. The results of this method are presented in the form of normalized static and impact pressures. This method is described in detail in reference 28.

Equivalent Body

The body-surface contour is rotated to the desired angle of attack by a simple rotation of the coordinates of the generating function of the forward shape. The method-of-characteristics solution was applied to the new axisymmetric body shape, generated from this contour.

Inouye-Lomax

Theoretical predictions for the blunt-nose (detached shock) configuration were obtained by using a numeric procedure developed by Inouye and Lomax (ref. 29). The method uses the Fuller blunt-body solution for the subsonic and transonic regions and the method-of-characteristics solution for the supersonic region.

Moeckel-Love

The procedure used to calculate Mach number profiles in the shear layer for the detached shock waves is outlined in reference 9. The procedure is based on Moeckel's method (ref. 30) with Love's modification for predicting the sonic point on the shock wave (ref. 31). The procedure uses a stream-tube (conservation of mass) approach. The local total pressure above the surface varies from the normal shock value at the surface to a value of total pressure behind the Mach wave.

REFERENCES

1. Tracy, Richard R.: Hypersonic Flow over a Yawed Circular Cone. Memo No. 69 (Contract No. DA-31-124-ARO(D)-33), Calif. Inst. of Tech., Aug. 1963.

2. Lankford, J. L.: Preliminary Results of Flow Surveys About an Inclined Body of Revolution at Mach Number 3.5. NAVORD Rep. 6708, U.S. Naval Ordnance Lab. (White Oak, Md.), Jan. 1960.

3. Creager, Marcus O.: The Effect of Leading-Edge Sweep and Surface Inclination on the Hypersonic Flow Field Over a Blunt Flat Plate. NASA MEMO 12-26-58A, 1959.

4. Brinich, Paul F.: Effect of Leading-Edge Geometry on Boundary-Layer Transition at Mach 3.1. NACA TN 3659, 1956.

5. Tendeland, Thorval; Nielsen, Helmer L.; and Fohrman, Melvin J.: The Flow Field Over Blunted Flat Plates and Its Effect on Turbulent Boundary-Layer Growth and Heat Transfer at a Mach Number of 4.7. NASA TN D-689, 1961.

6. Kubota, Toshi: Investigation of Flow Around Simple Bodies in Hypersonic Flow. Ph. D. Thesis, Calif. Inst. of Tech., 1957.

7. Banner, Richard D.; Kuhl, Albert E.; and Quinn, Robert D.: Preliminary Results of Aerodynamic Heating Studies on the X-15 Airplane. NASA TM X-638, 1962.

8. Watts, Joe D.; and Banas, Ronald P.: X-15 Structural Temperature Measurements and Calculations for Flights to Maximum Mach Numbers of Approximately 4, 5, and 6. NASA TM X-883, 1963.

9. Quinn, Robert D.; and Kuhl, Albert E.: Comparison of Flight-Measured and Calculated Turbulent Heat Transfer on the X-15 Airplane at Mach Numbers From 2.5 to 6.0 at Low Angles of Attack. NASA TM X-939, 1964.

10. Pyle, Jon S.: Comparison of Flight Pressure Measurements With Wind-Tunnel Data and Theory for the Forward Fuselage of the X-15 Airplane at Mach Numbers From 0.8 to 6.0. NASA TN D-2241, 1964.

11. Banas, Ronald P.: Comparison of Measured and Calculated Turbulent Heat Transfer in a Uniform and Nonuniform Flow Field on the X-15 Upper Vertical Fin at Mach Numbers of 4.2 and 5.3. NASA TM X-1136, 1965.

12. Osborne, Robert S.; and Stafford, Virginia C.: Basic Pressure Measurements on a 0.0667-Scale Model of the North American X-15 Research Airplane at Transonic Speeds. NASA TM X-344, 1960.

13. Anon.: Wind Tunnel Tests and Model Information for 0.067-Scale Heat Transfer and Pressure Model of the X-15 Research Airplane. Rept. No. NA-56-1226, North American Aviation, Inc., Nov. 29, 1956.

14. Wolowicz, Chester H.; and Gossett, Terrence D.: Operational and Performance Characteristics of the X-15 Spherical, Hypersonic Flow-Direction Sensor. NASA TN D-3070, 1965.

15. Hill, J. A. F.; Baron, J. R.; Schindel, L. H.; and Markham, J. R.: Mach Number Measurements in High-Speed Wind Tunnels. AGARDograph 22, Oct. 1956.

16. Gracey, William: Wind-Tunnel Investigation of a Number of Total-Pressure Tubes at High Angles of Attack. Subsonic, Transonic, and Supersonic Speeds. NACA Rept. 1303, 1957. (Supersedes NACA TN 3641.)

17. Korkegi, Robert H.; and Mannes, Robert L.: Investigation of Free-Stream Pressure and Stagnation Pressure Measurement From Transonic and Supersonic Aircraft. WADC Tech. Rep. 55-238 (Contract No. AF 33(616)-2396), Wright Air Dev. Center, U.S. Air Force, Mar. 1955.

18. Ludwig, G. R.: Effects of Probe Size on Measurements in a Laminar Boundary Layer in Supersonic Flow. UTIA Tech. Note No. 9, Inst. of Aerophysics, Univ. of Toronto, Nov. 1956.

19. Wilson, R. E.; and Young, E. C.: Aerodynamic Interference of Pitot Tubes in a Turbulent Boundary Layer at Supersonic Speed. DRL-228, Defense Research Lab., Univ. of Texas, Dec. 6, 1949.

20. Larson, Terry J.; and Webb, Lannie D.: Calibrations and Comparisons of Pressure-Type Airspeed-Altitude Systems of the X-15 Airplane From Subsonic to High Supersonic Speeds. NASA TN D-1724, 1963.

21. Rippey, J.: Flow-Field Investigation of a 0.0667-Scale Model of the X-15 Research Vehicle at Mach 4, 6, and 8. Tech. Doc. Rep. No. AEDC-TDR-64-201, Arnold Eng. Dev. Center, Oct. 1964.

22. Anon.: Test Facilities Handbook. Fifth ed., vol. 4, Arnold Eng. Dev. Center, July 1963.

23. Anon.: Manual for Users of the Unitary Plan Wind Tunnel Facilities of the National Advisory Committee for Aeronautics. NACA, 1956.

24. Hodge, B. Leon; and Burbank, Paige B.: Pressure Distribution of a 0.0667-Scale Model of the X-15 Airplane for an Angle-of-Attack Range of 0° to 28° at Mach Numbers of 2.30, 2.88, and 4.65. NASA TM X-275, 1960.

25. Ashby, George C., Jr.; and Goldberg, Theodore J.: Application of Generalized Newtonian Theory to Three-Dimensional Sharp-Nose Shock-Detached Bodies at Mach 6 for Angles of Attack up to 25°. NASA TN D-2550, 1965.

26. Ehret, Dorris M.: Accuracy of Approximate Methods for Predicting, Pressures on Pointed Nonlifting Bodies of Revolution in Supersonic Flow. NACA TN 2764, 1952.

27. Ames Research Staff: Equation, Tables, and Charts for Compressible Flow. NACA Rept. 1135, 1953. (Supersedes NACA TN 1428.)

28. Ferri, Antonio: Application of the Method of Characteristics to Supersonic Rotational Flow. NACA Rept. 841, 1946.

29. Inouye, Mamoru; Rakich, John V.; and Lomax, Harvard: A Description of Numerical Methods and Computer Programs for Two-Dimensional and Axisymmetric Supersonic Flow Over Blunt-Nosed and Flared Bodies. NASA TN D-2970, 1965.

30. Moeckel, W. E.: Approximate Method for Predicting Form and Location of Detached Shock Waves Ahead of Plane or Axially Symmetric Bodies. NACA TN 1921, 1949.

31. Love, Eugene S.: A Reexamination of the Use of Simple Concepts for Predicting the Shape and Location of Detached Shock Waves. NACA TN 4170, 1957.

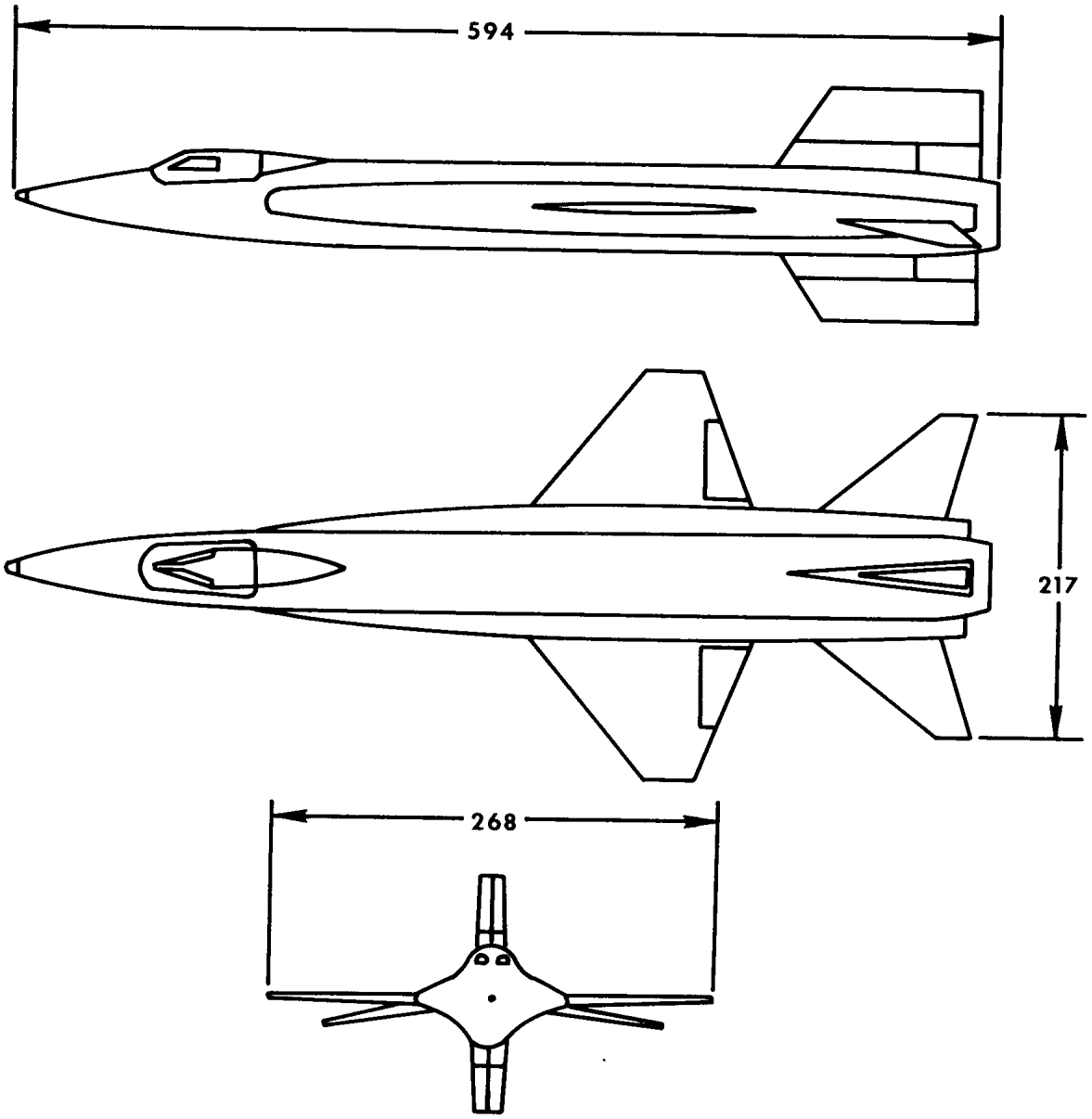

Figure 1.– Three-view drawing of the X-15 with ball nose. All dimensions in inches.

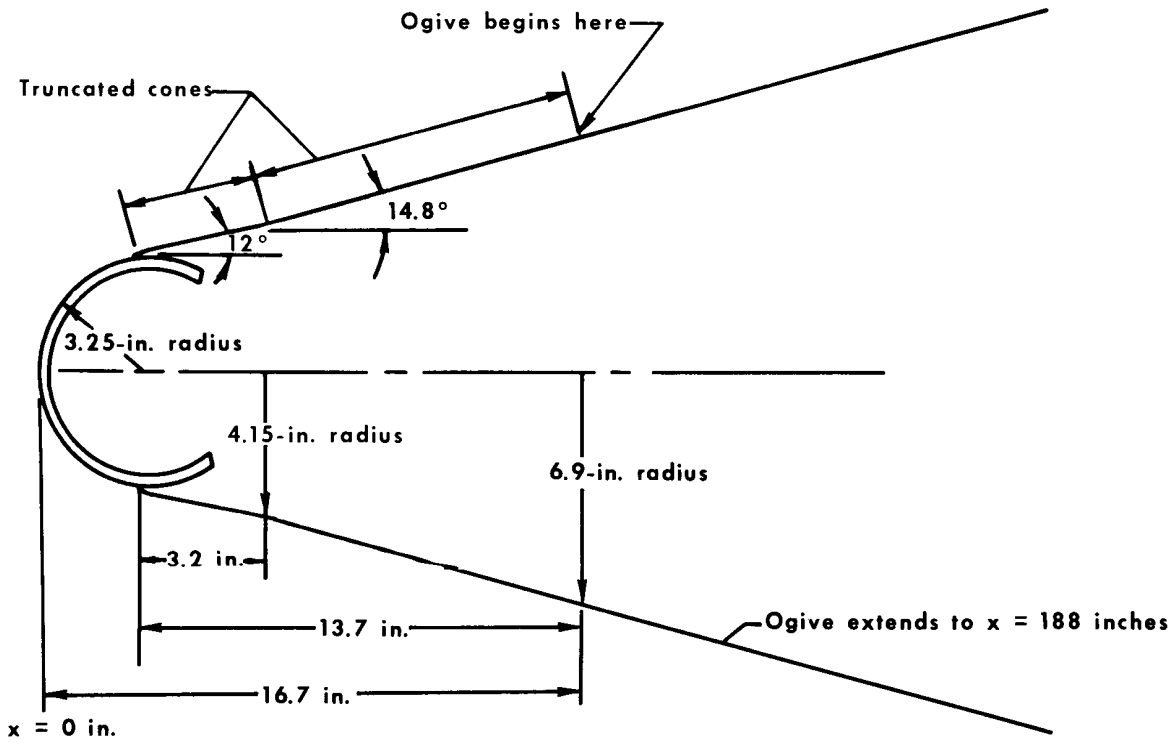

(a) Airplane forebody.

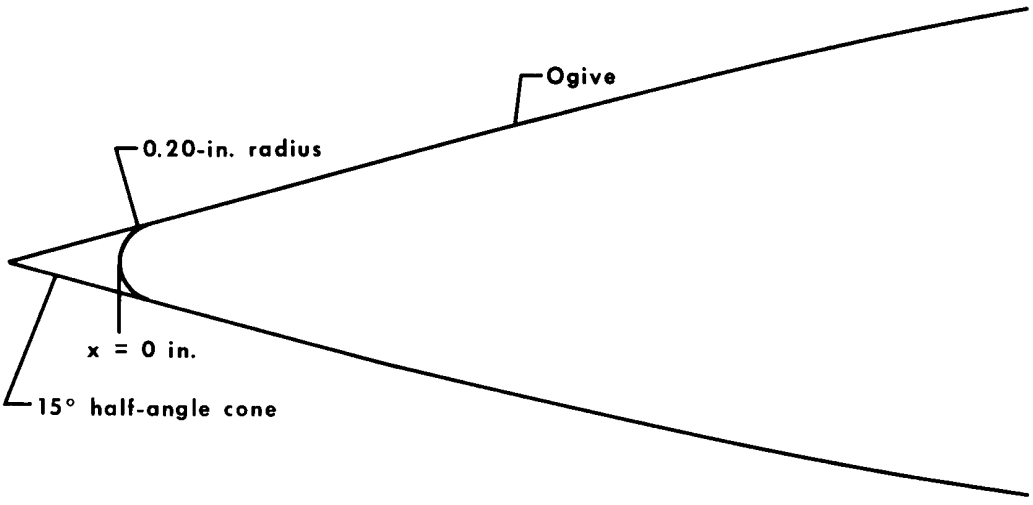

(b) Forebody of the 1/15-scale heat-transfer and pressure model.

Figure 2.– Dimensions of X-15 forward fuselage.

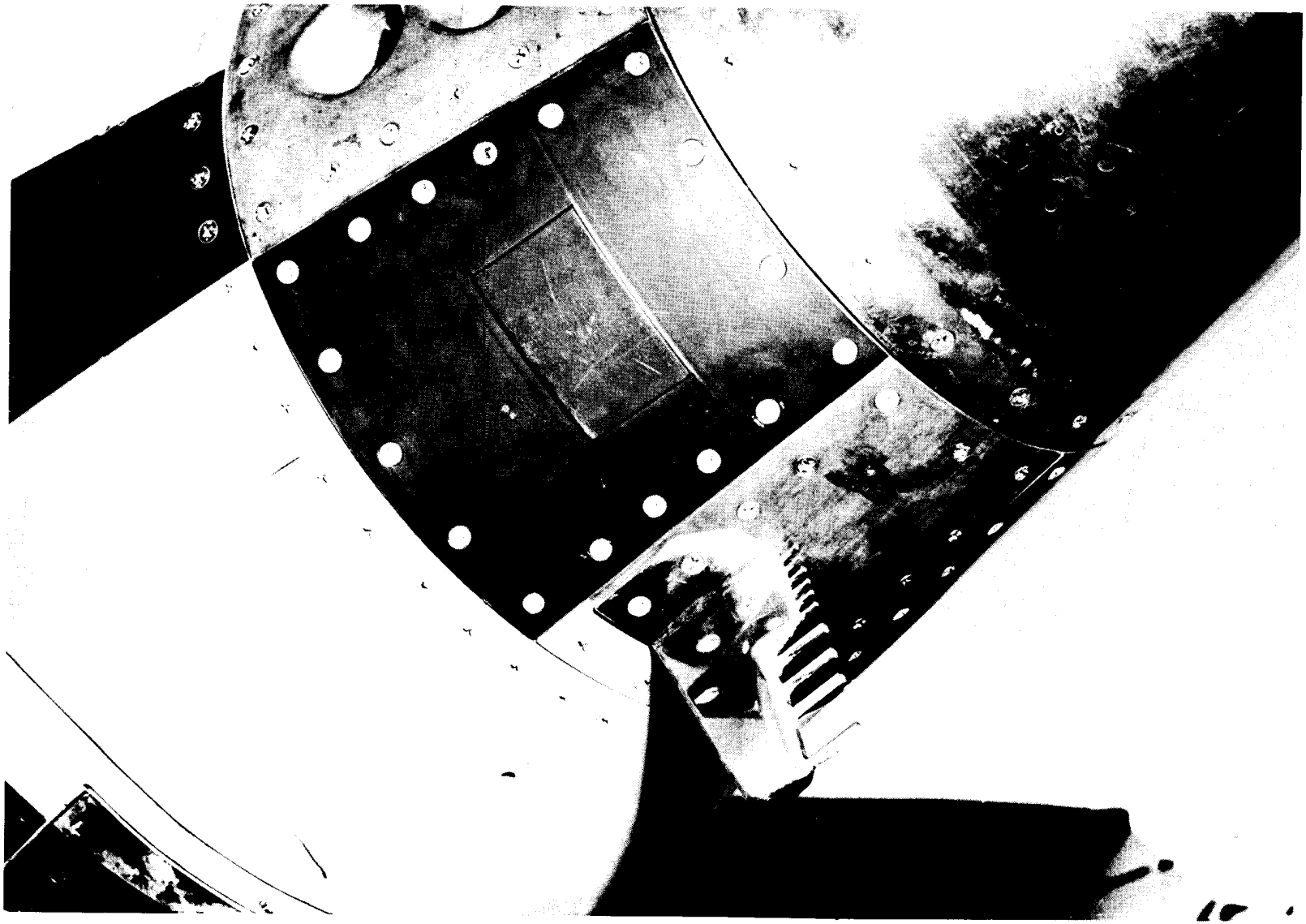

Figure 3.– Typical rake installation on the lower centerline of the X-15 airplane. x = 20 inches. E-11753

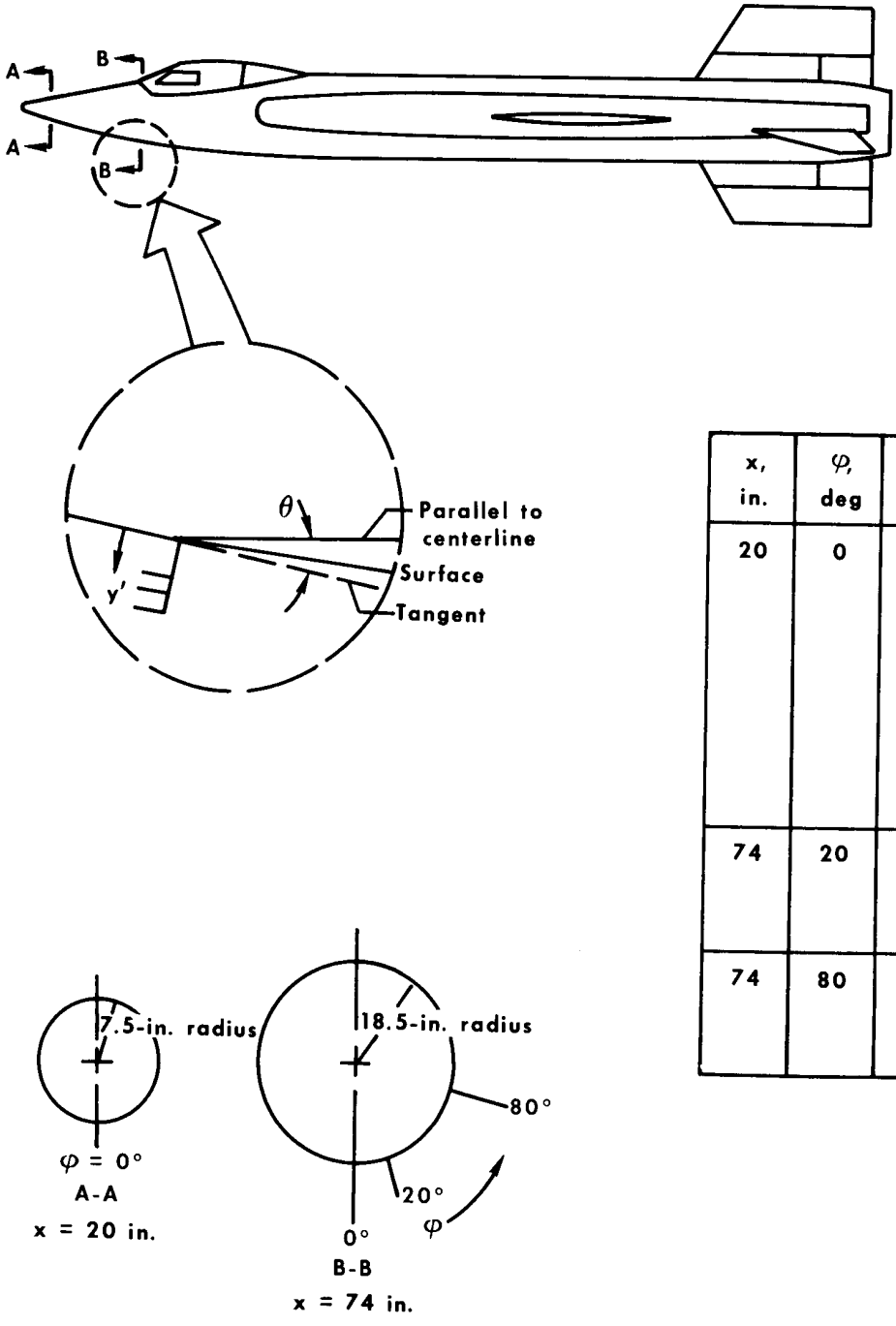

x, in.	φ, deg	θ, deg	y', in.
20	0	13.5	0.25
			.50
			.75
			1.00
			1.25
			1.50
			2.00
			3.00
74	20	11.5	2.00
			3.00
			4.00
74	80	11.5	2.00
			3.00
			4.00

Figure 4.– Sketch of rake locations and local geometry on the X-15 airplane.

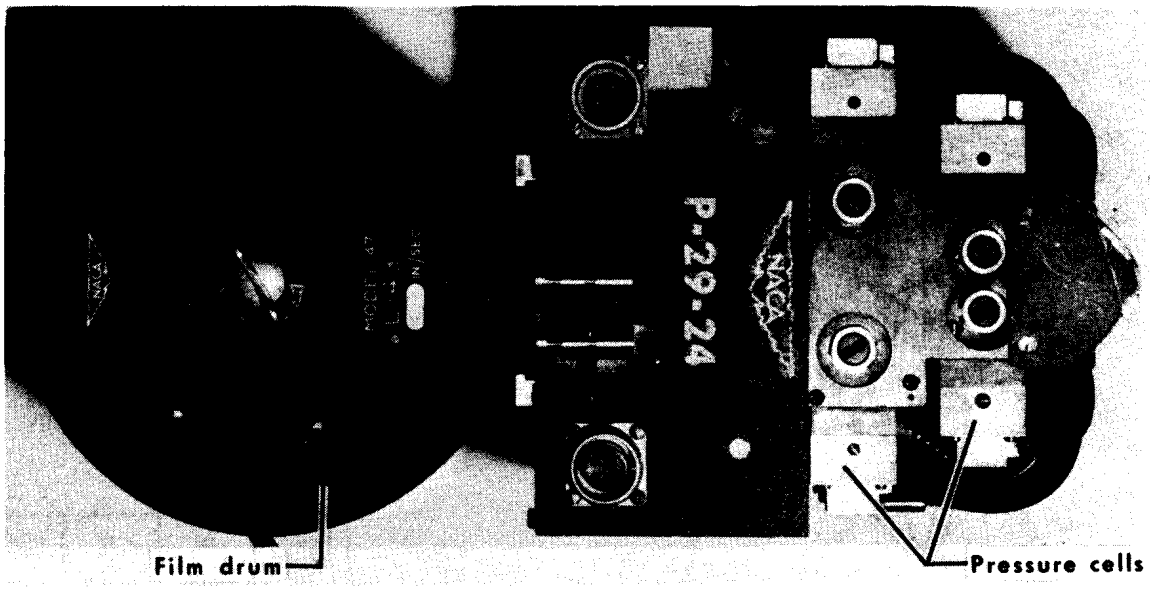

(a) NACA manometer. Length, 16.3 inches; maximum width, 7.4 inches.

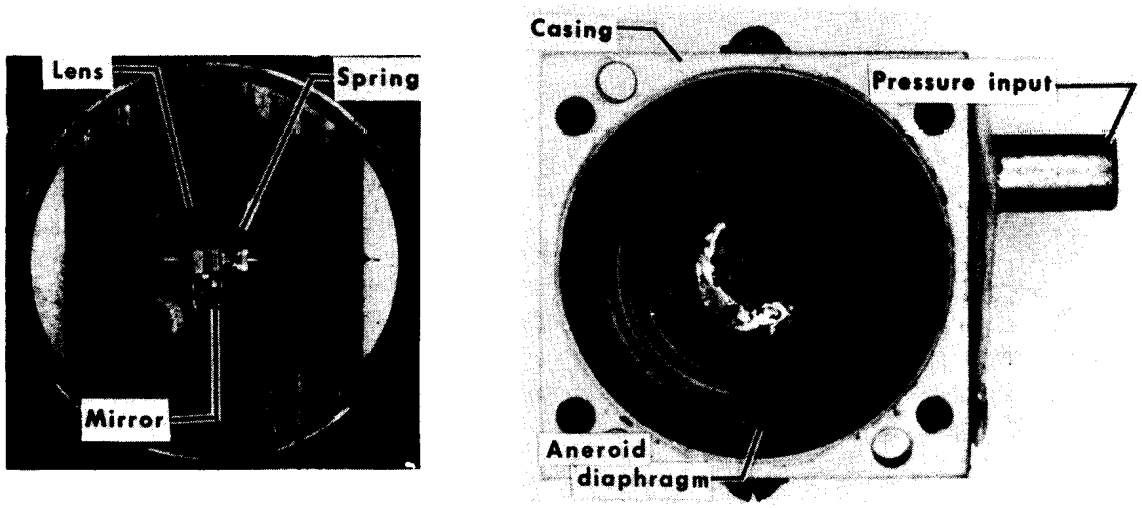

(b) Detailed view of an absolute-pressure cell.

Figure 5.— A standard NACA manometer and a detailed view of an absolute-pressure-reading manometer cell.

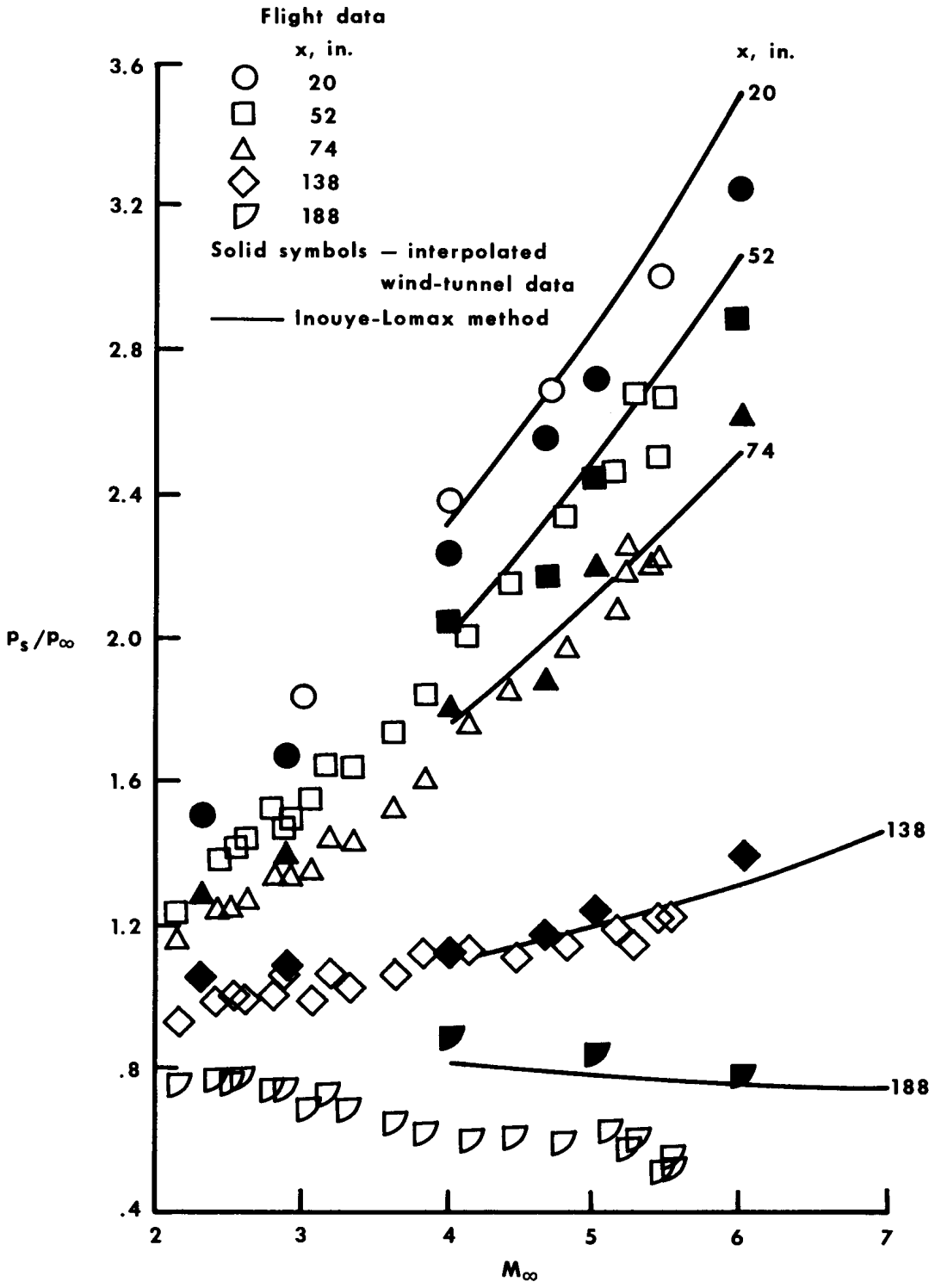

Figure 6.– Variation of surface static pressure with free-stream Mach number at discrete locations along the lower centerline of the X-15 ogival surface. $\alpha = 0°$.

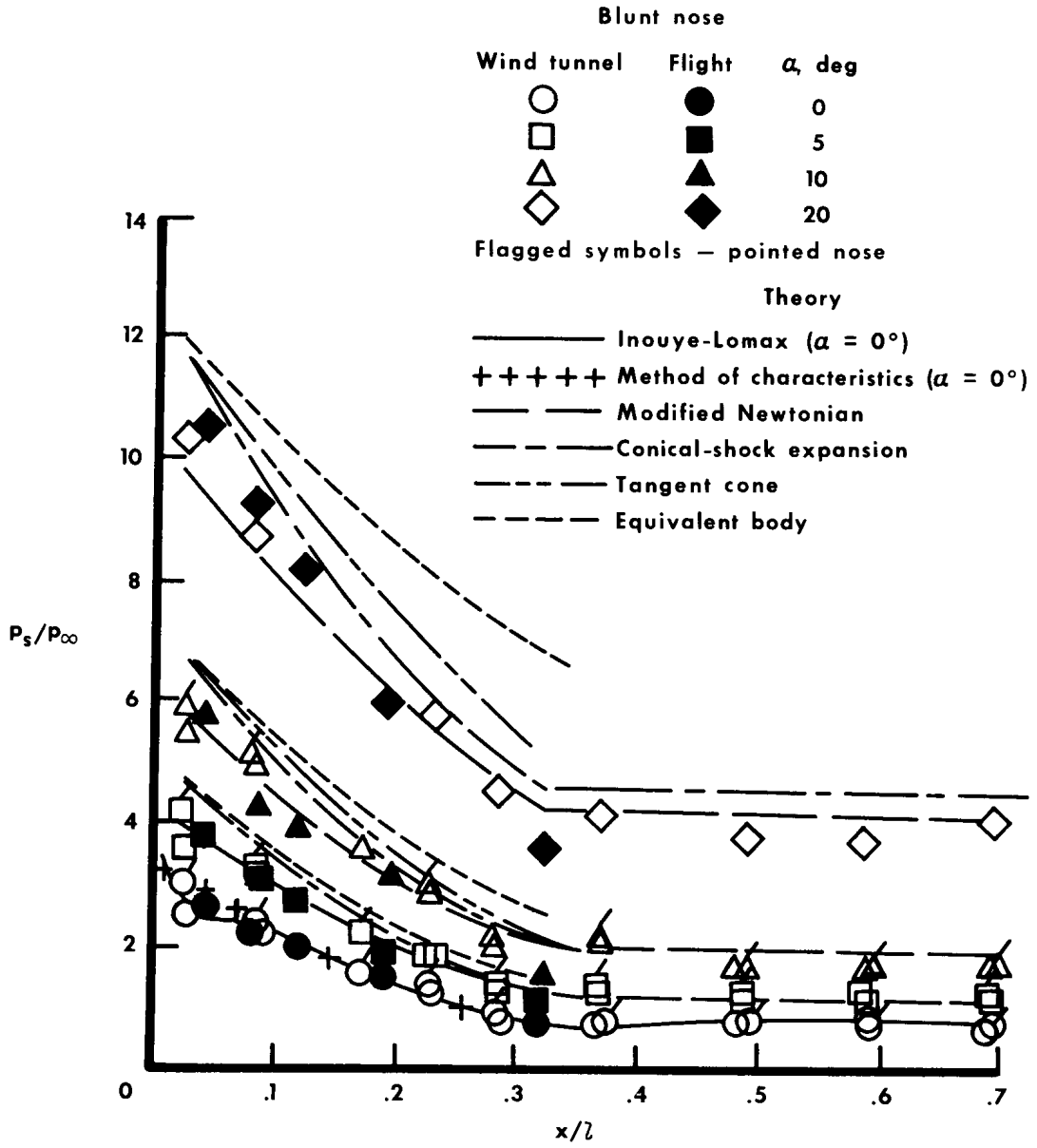

(a) $M_\infty = 4.7$.

Figure 7.— Effect of angle of attack on the distribution of the longitudinal surface pressure along the lower centerline of the X-15.

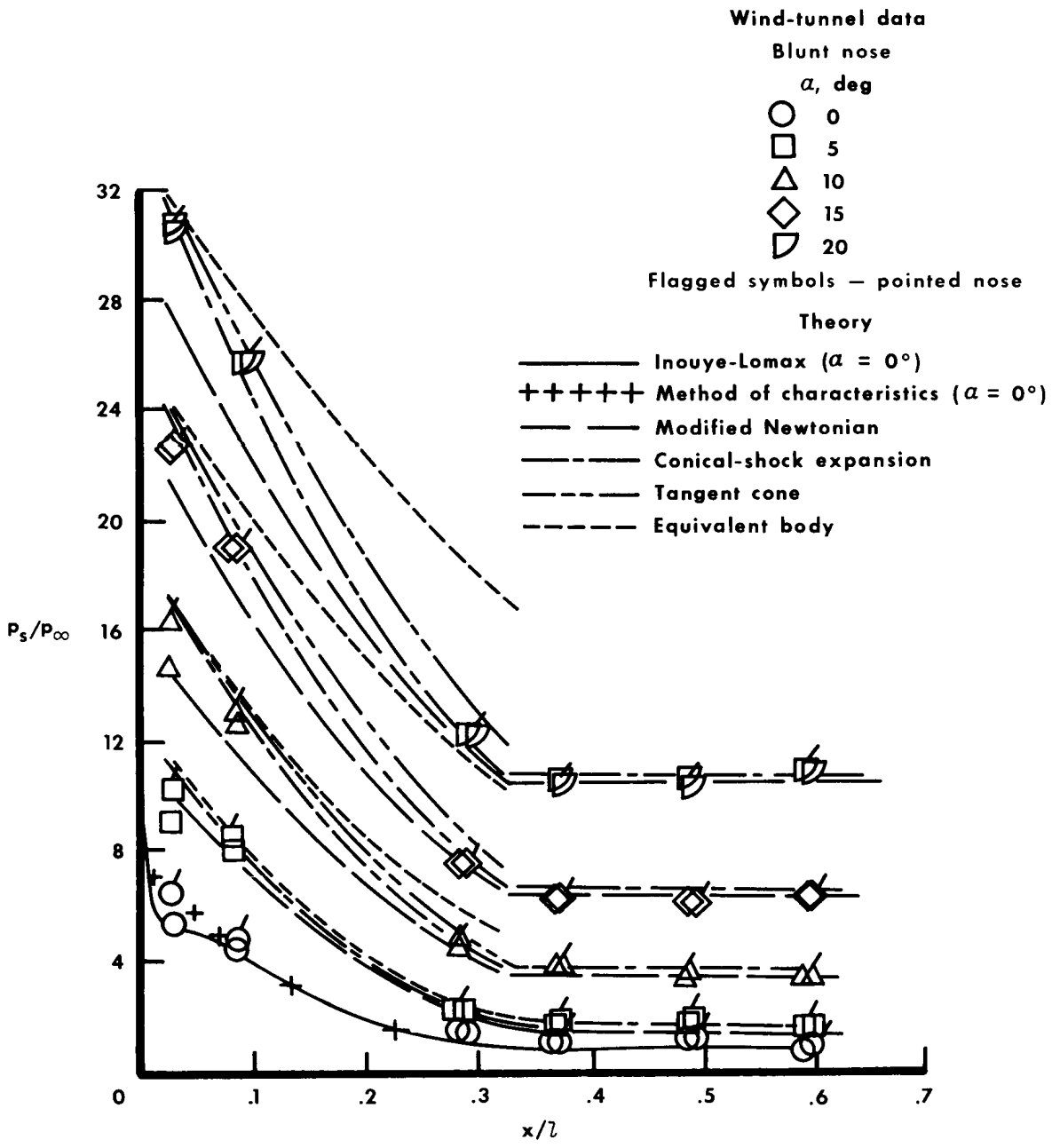

(b) $M_\infty = 8.0$.

Figure 7.– Concluded.

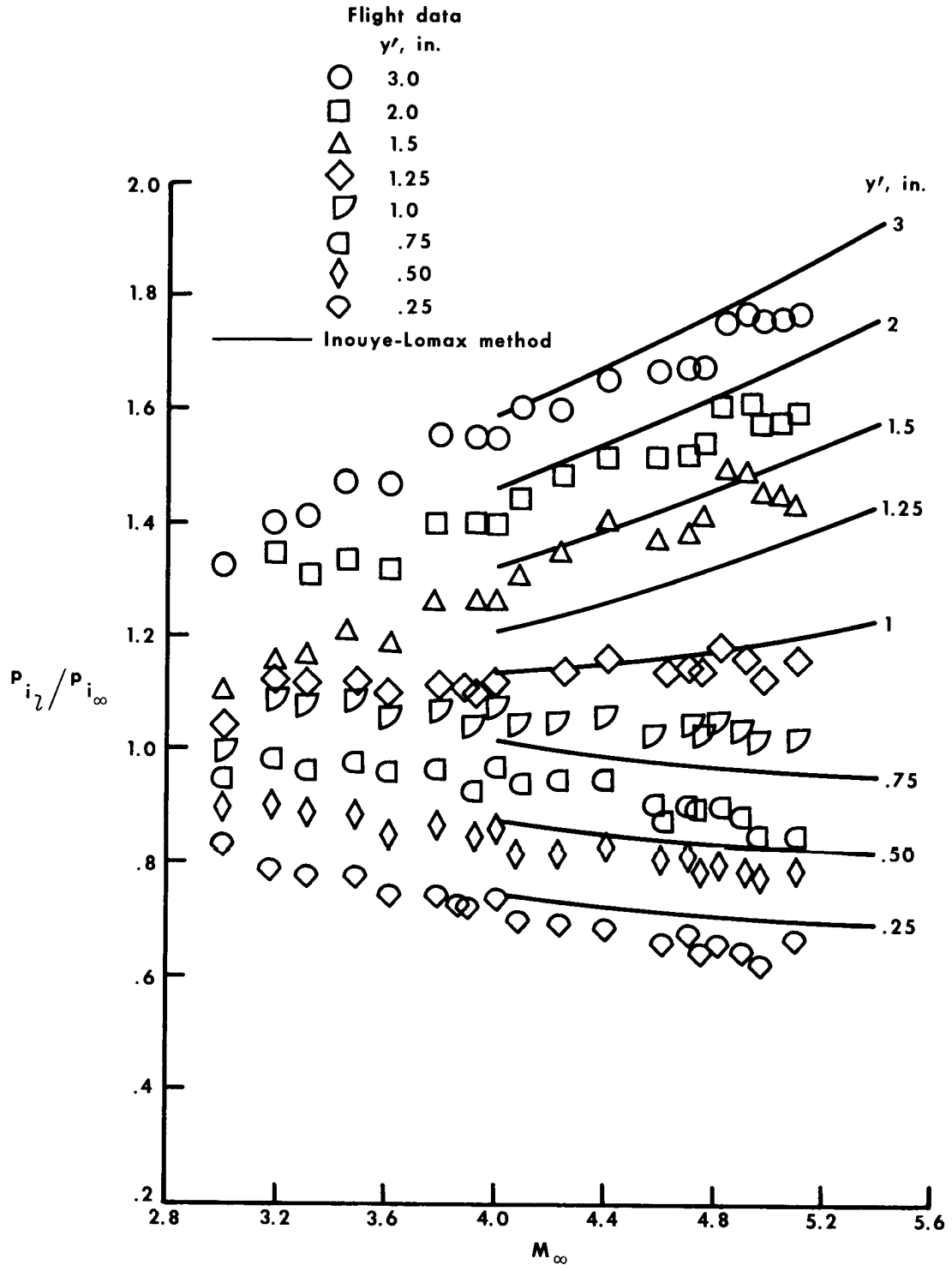

(a) x = 20 inches.

Figure 8.– Effect of free-stream Mach number on the measured impact pressure for $\alpha = 0°$.

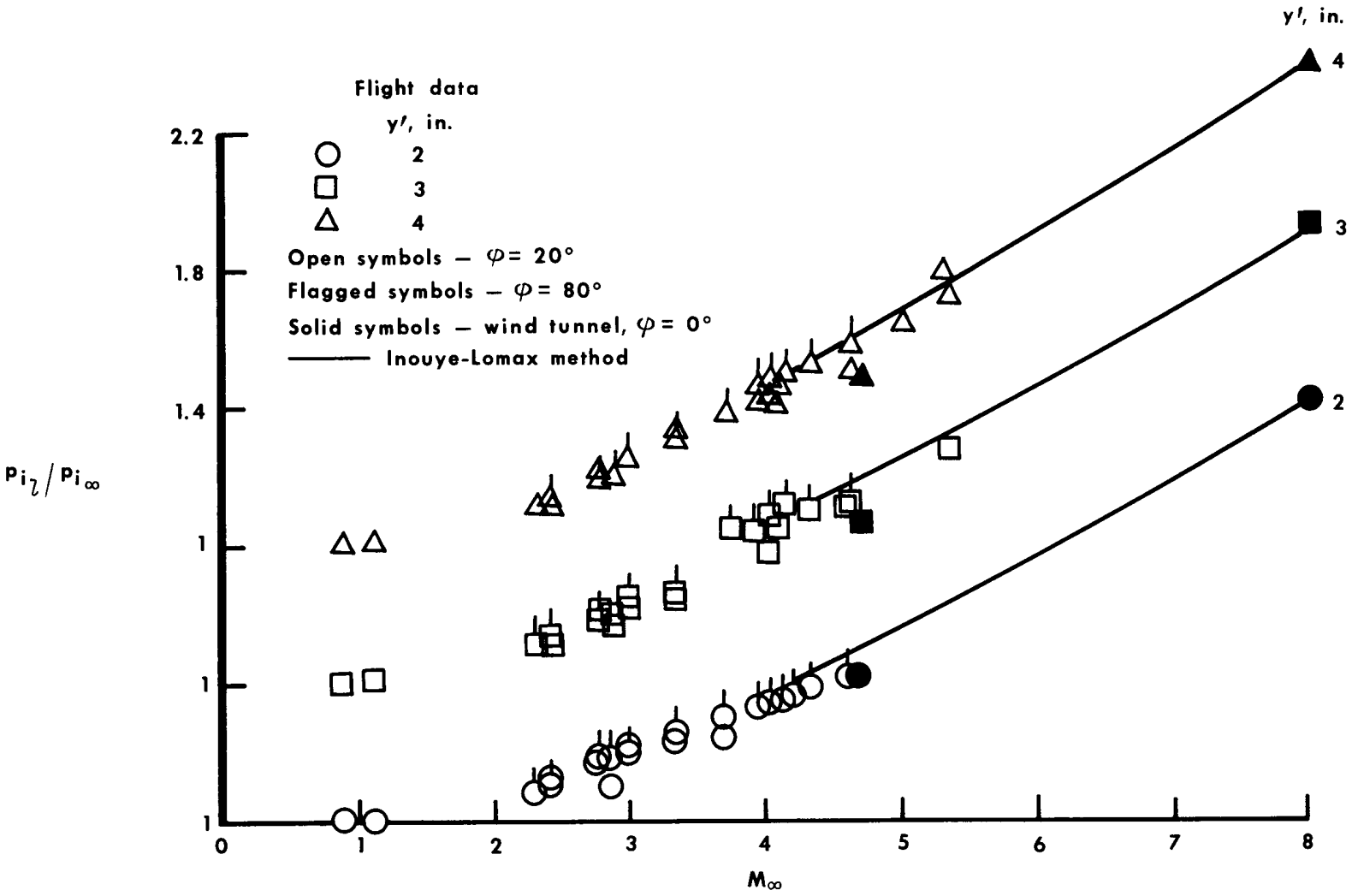

(b) x = 74 inches.

Figure 8.– Concluded.

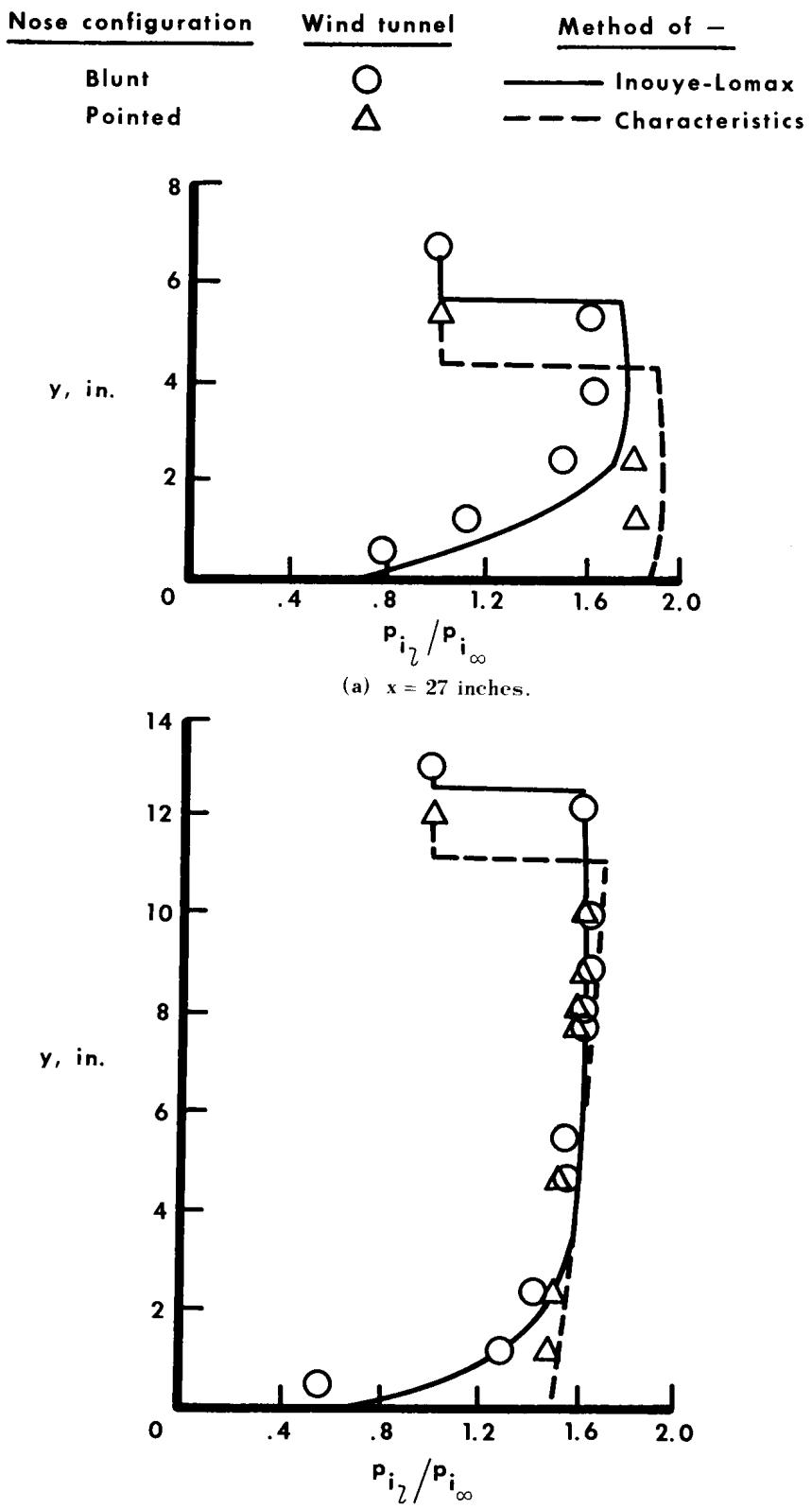

(a) x = 27 inches.

(b) x = 74 inches.

Figure 9.— Effect of nose configuration on the impact-pressure distribution from the surface through the shock. $\alpha = 0°$; $M_\infty = 4.7$.

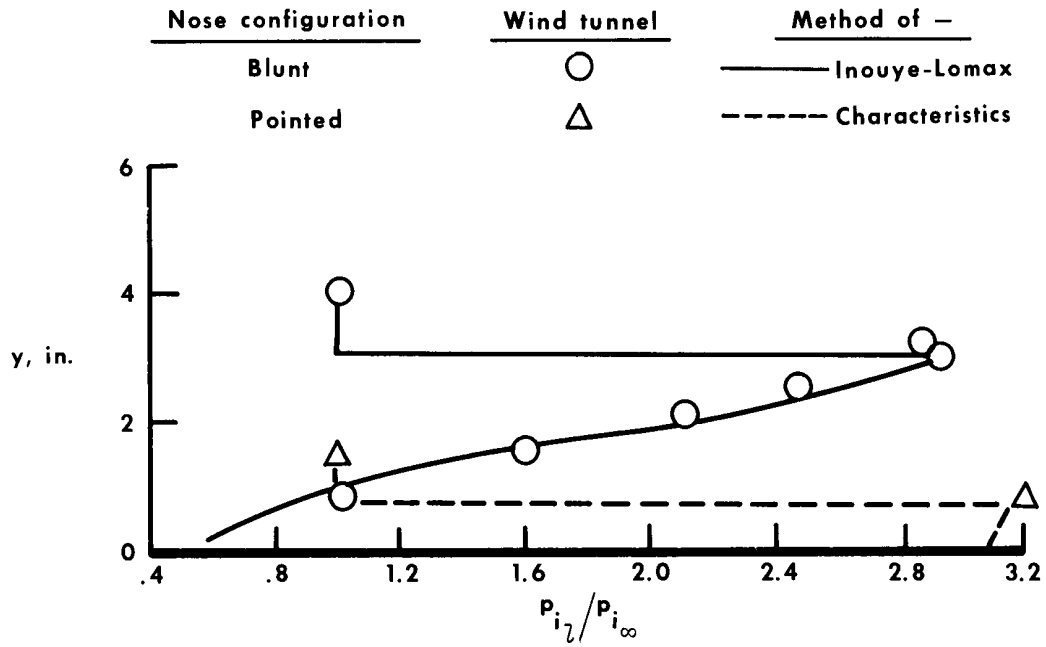

(a) x = 15 inches.

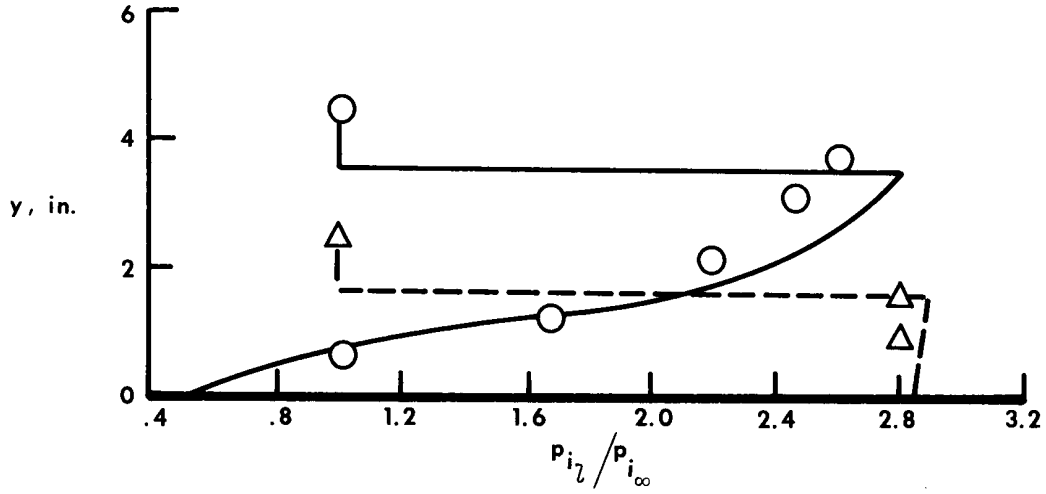

(b) x = 27 inches.

Figure 10.– Effect of nose configuration on impact-pressure distribution from the surface through the shock. $\alpha = 0^\circ$, $M_\infty = 8.0$.

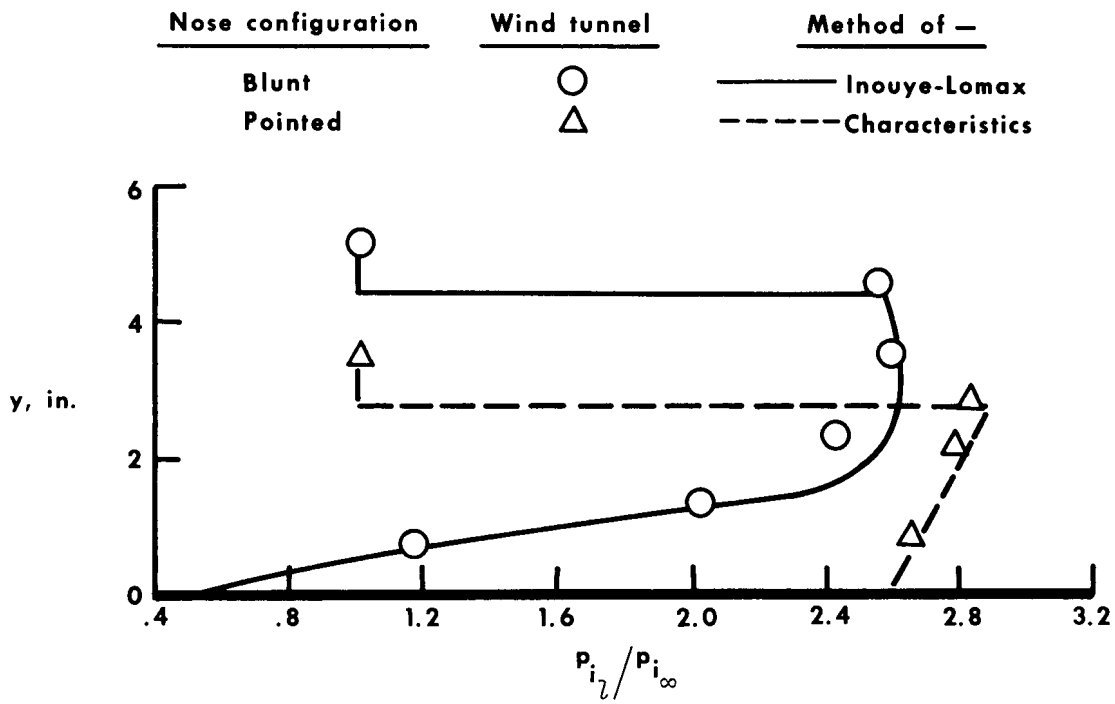

(c) x = 45 inches.

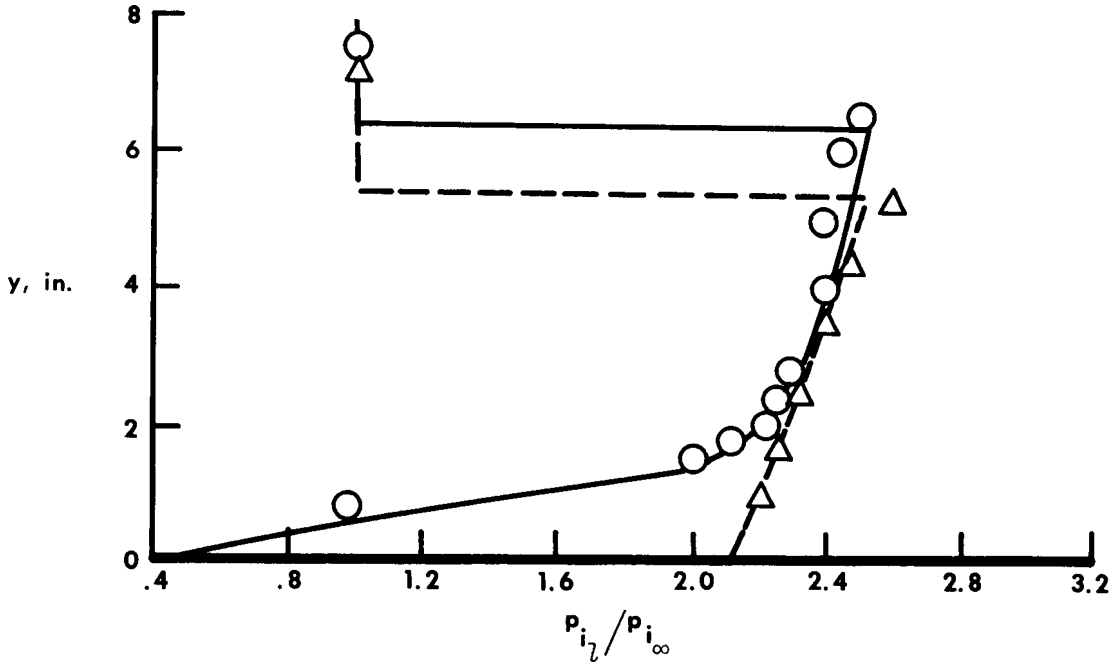

(d) x = 74 inches.

Figure 10.– Concluded.

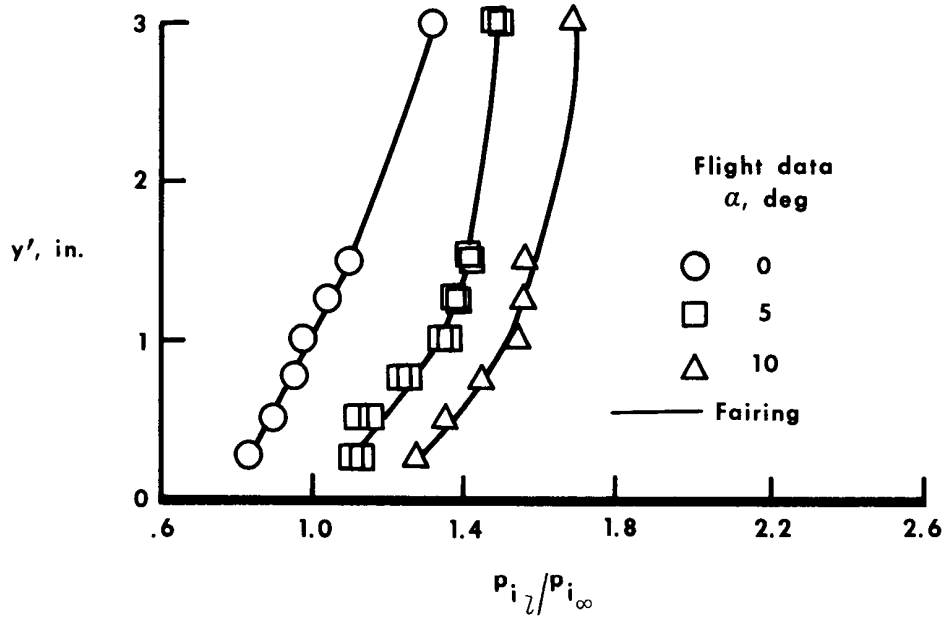

(a) $M_\infty = 3.0$.

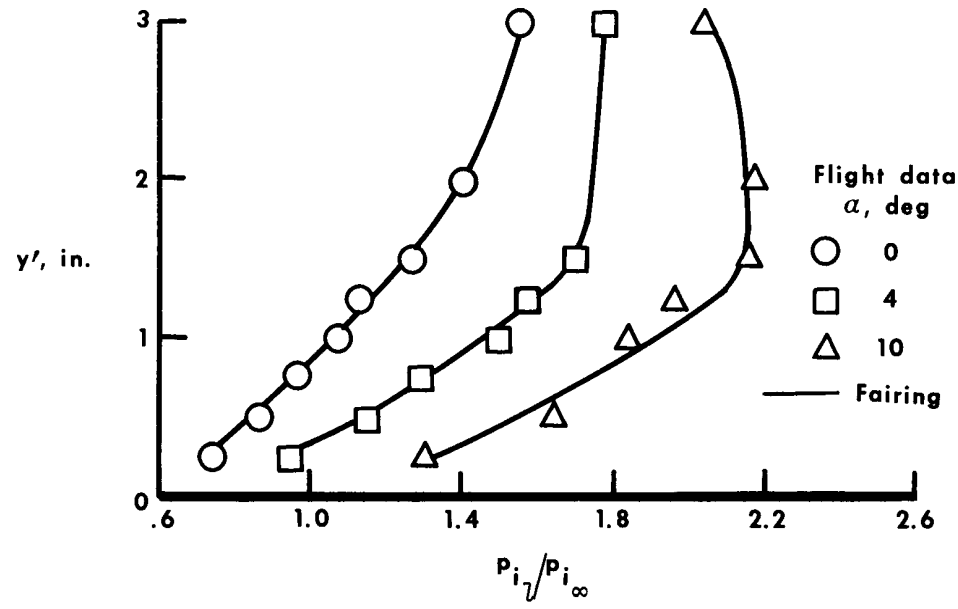

(b) $M_\infty = 4.0$.

Figure 11.– Effect of angle of attack on the impact-pressure distribution on the lower centerline of the X-15. x = 20 inches.

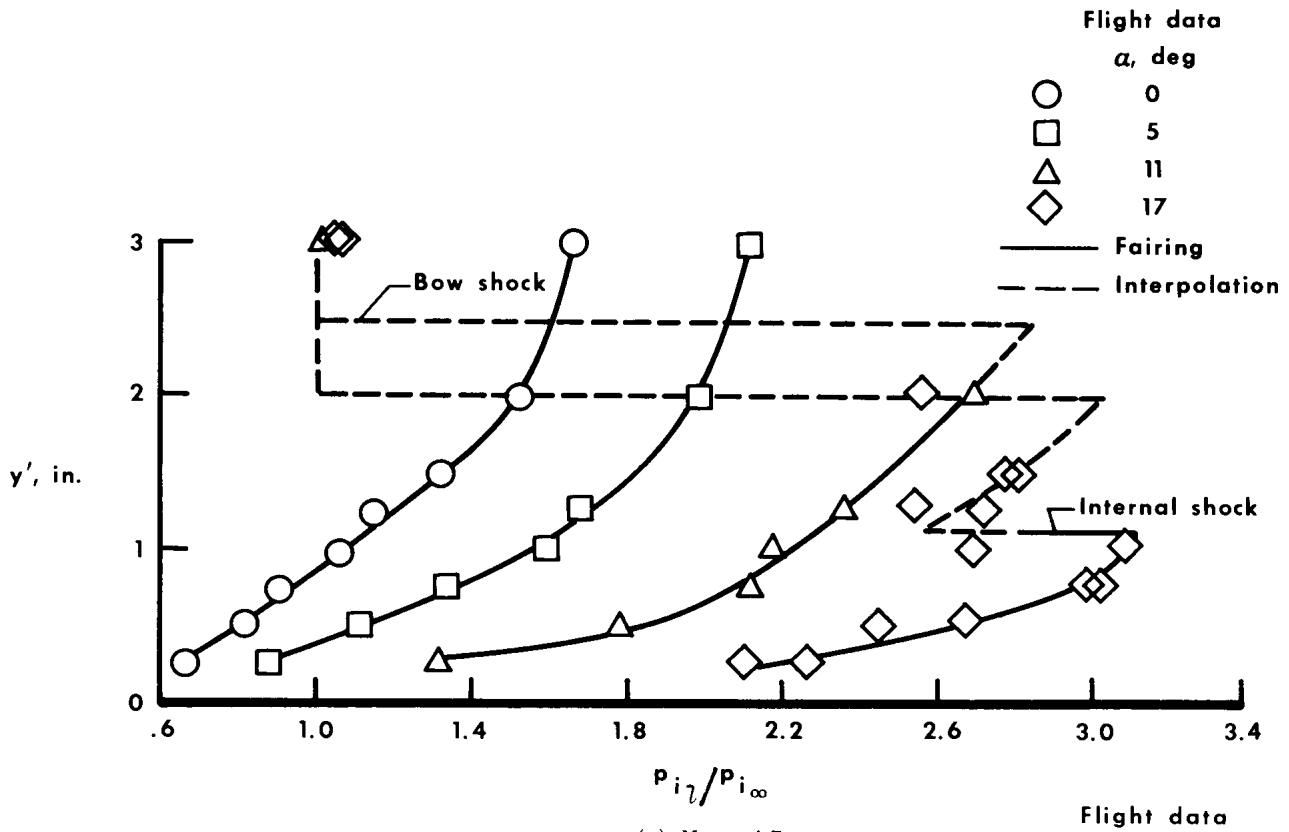

(c) $M_\infty = 4.7$.

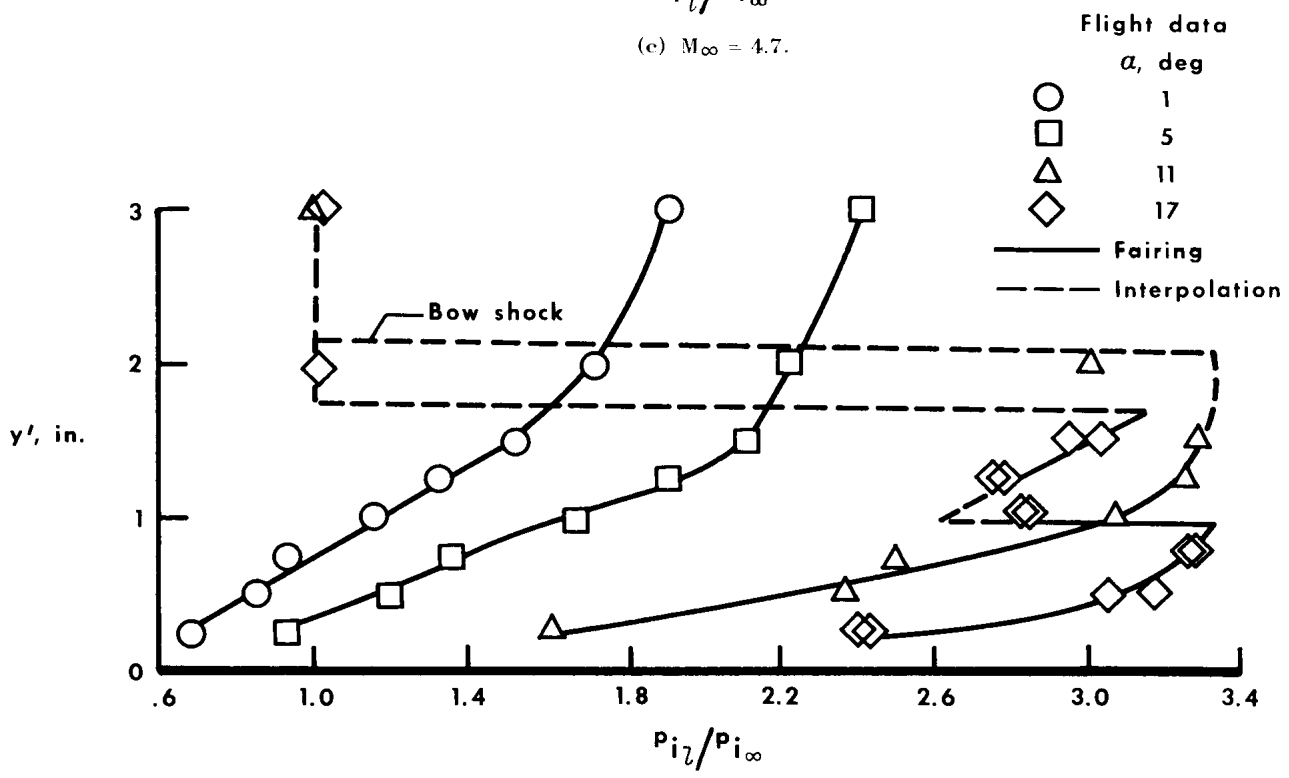

(d) $M_\infty = 5.4$.

Figure 11.– Concluded.

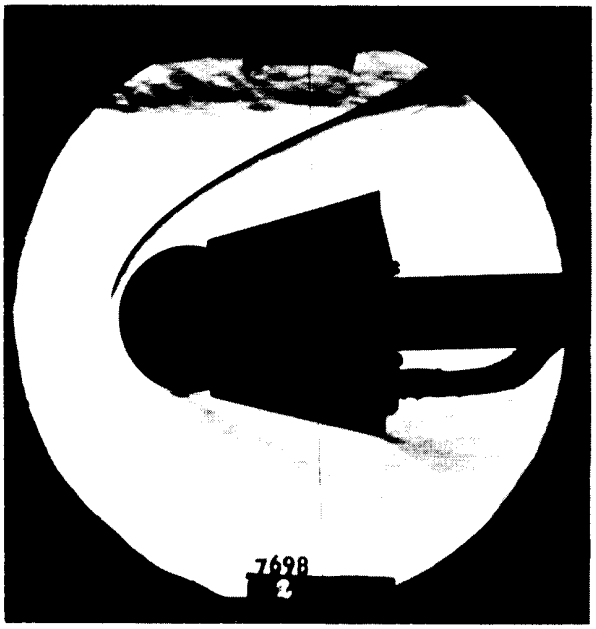

(a) $\alpha = 0^\circ$.

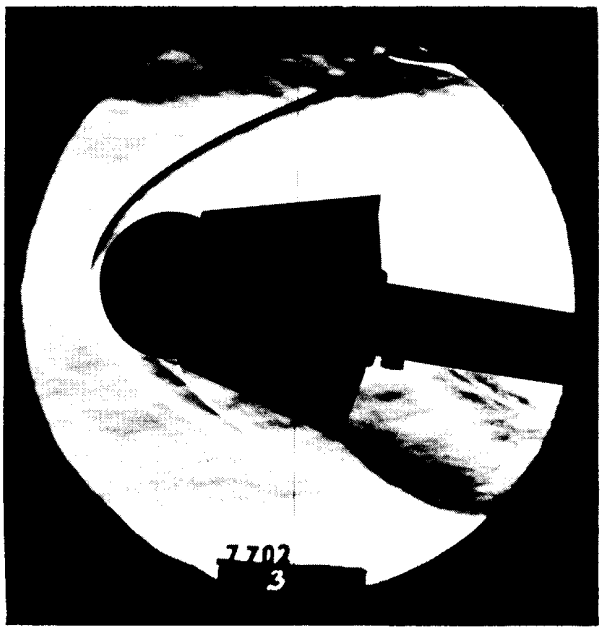

(b) $\alpha = 8^\circ$.

(c) $\alpha = 16^\circ$.

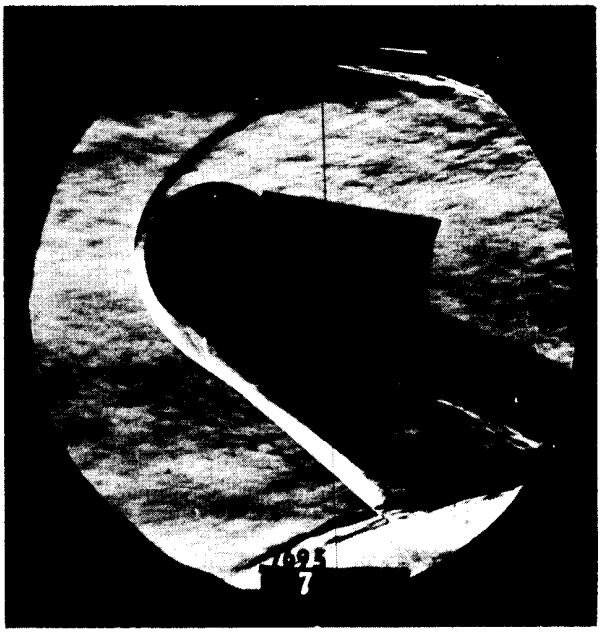

(d) $\alpha = 24^\circ$.

Figure 12.– Schlieren photographs of flow-direction-sensor configuration at $M_\infty = 6.8$.

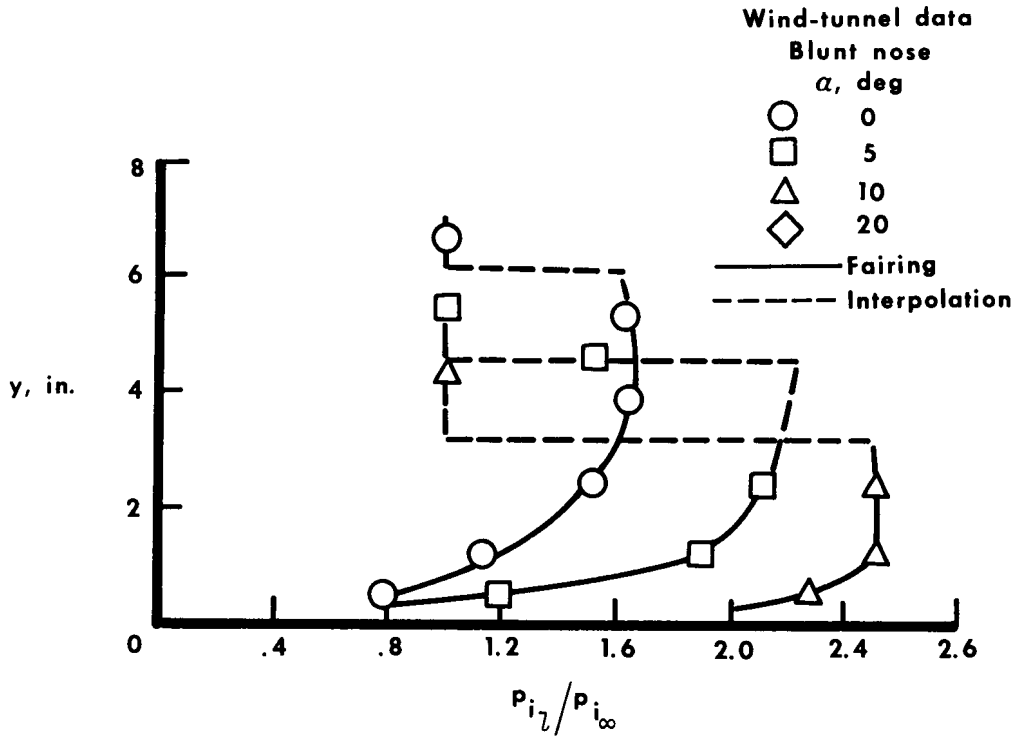

(a) x = 27 inches.

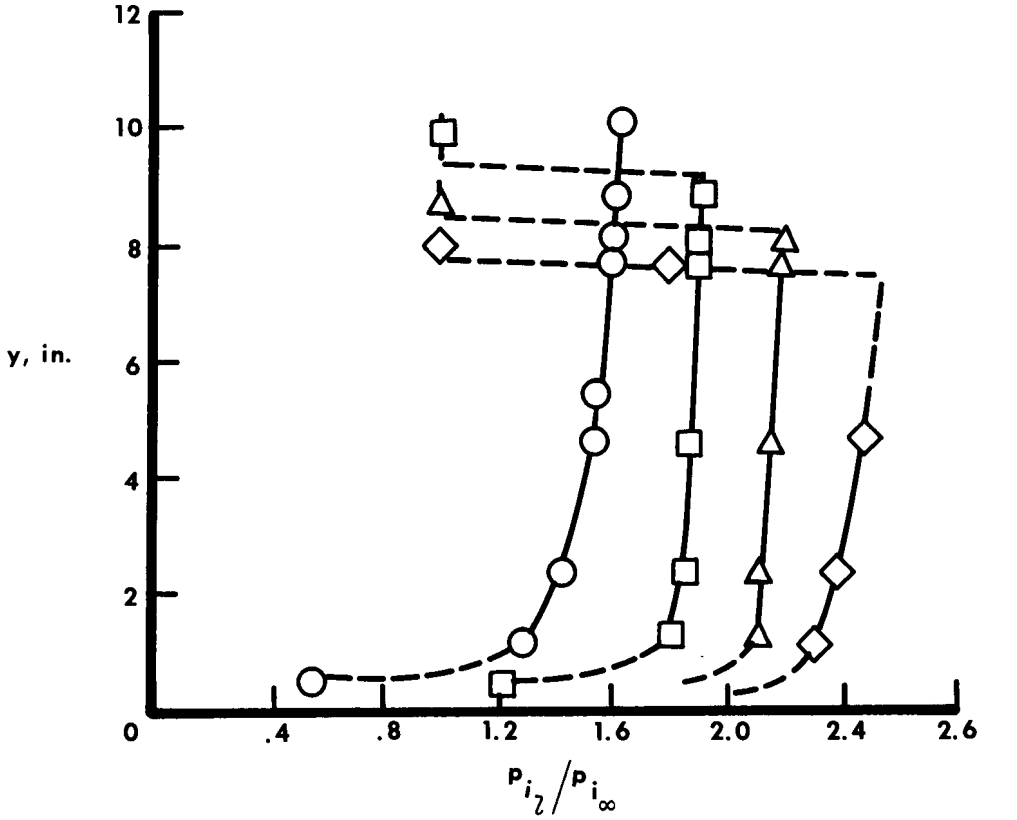

(b) x = 74 inches.

Figure 13.– Effect of angle of attack on the impact-pressure distribution through the flow field below the lower centerline of the X-15 1/15-scale model. M_∞ = 4.7.

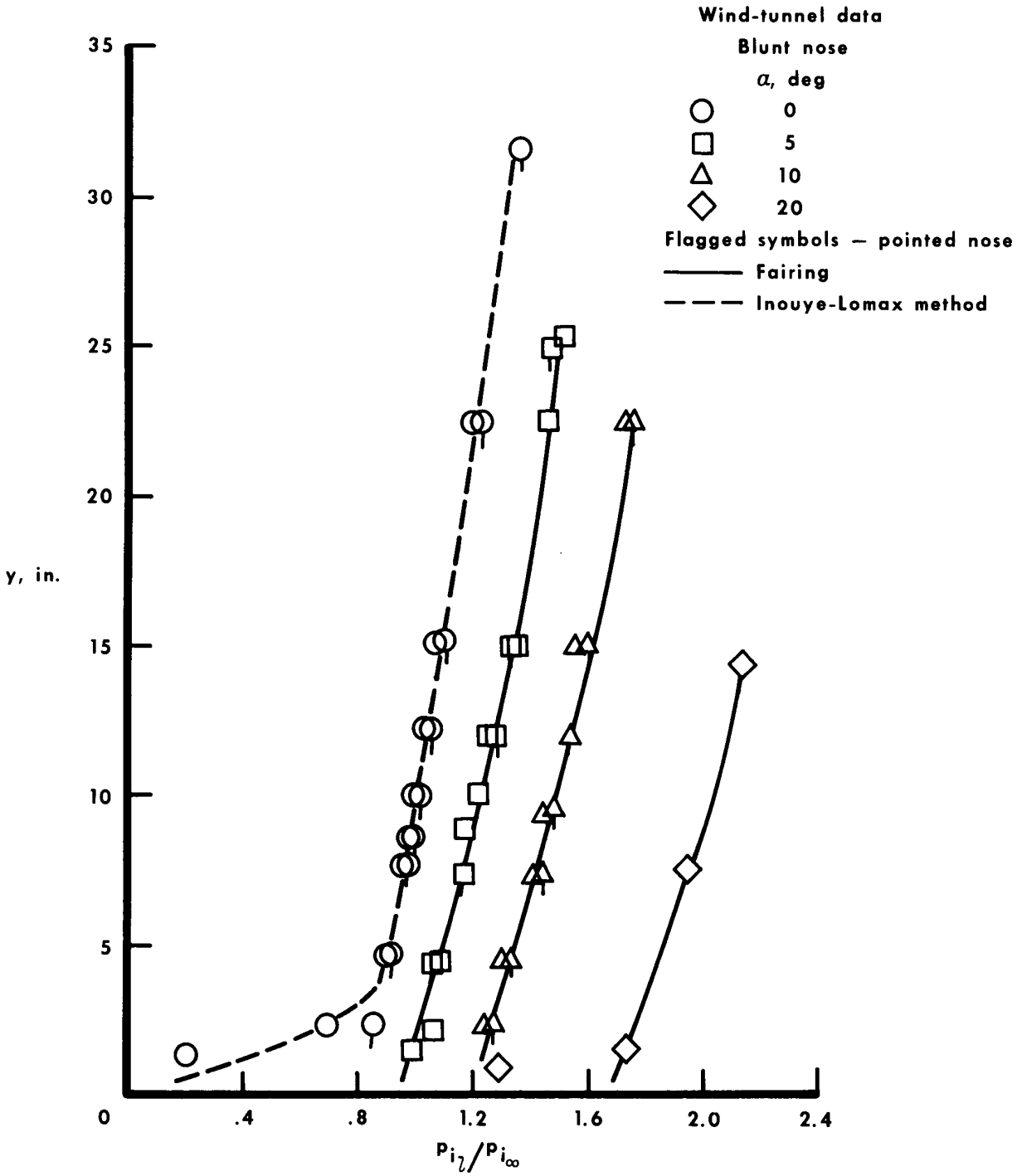

(c) x = 192 inches.

Figure 13.– Concluded.

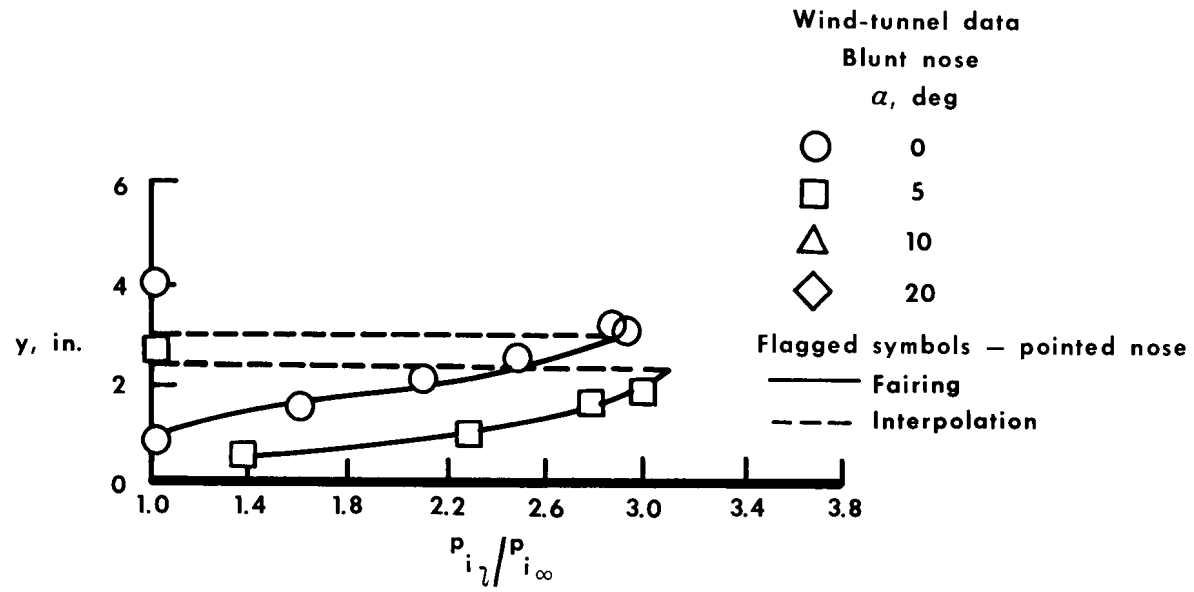

(a) x = 15 inches.

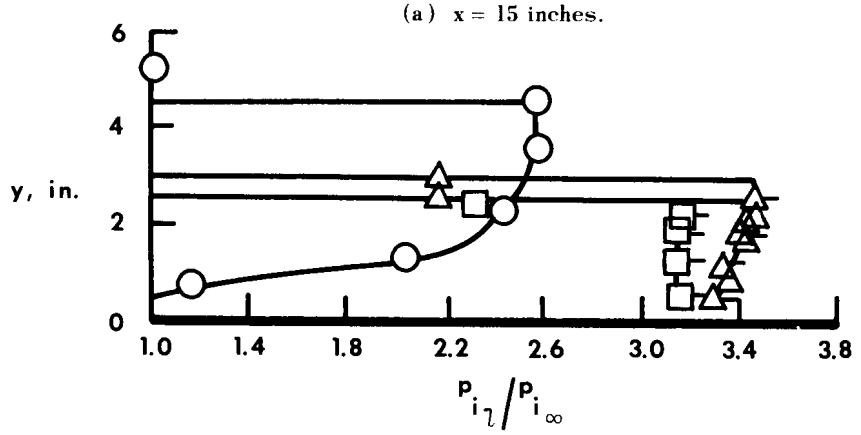

(b) x = 45 inches.

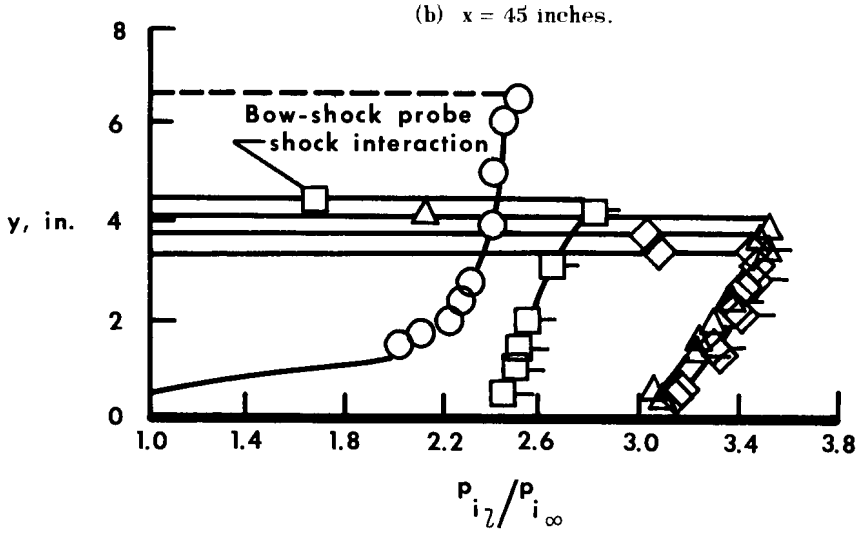

(c) x = 74 inches.

Figure 14.– Effect of angle of attack on the impact-pressure distribution through the flow field below the lower centerline of the 1/15-scale model. $M_\infty = 8.0$.

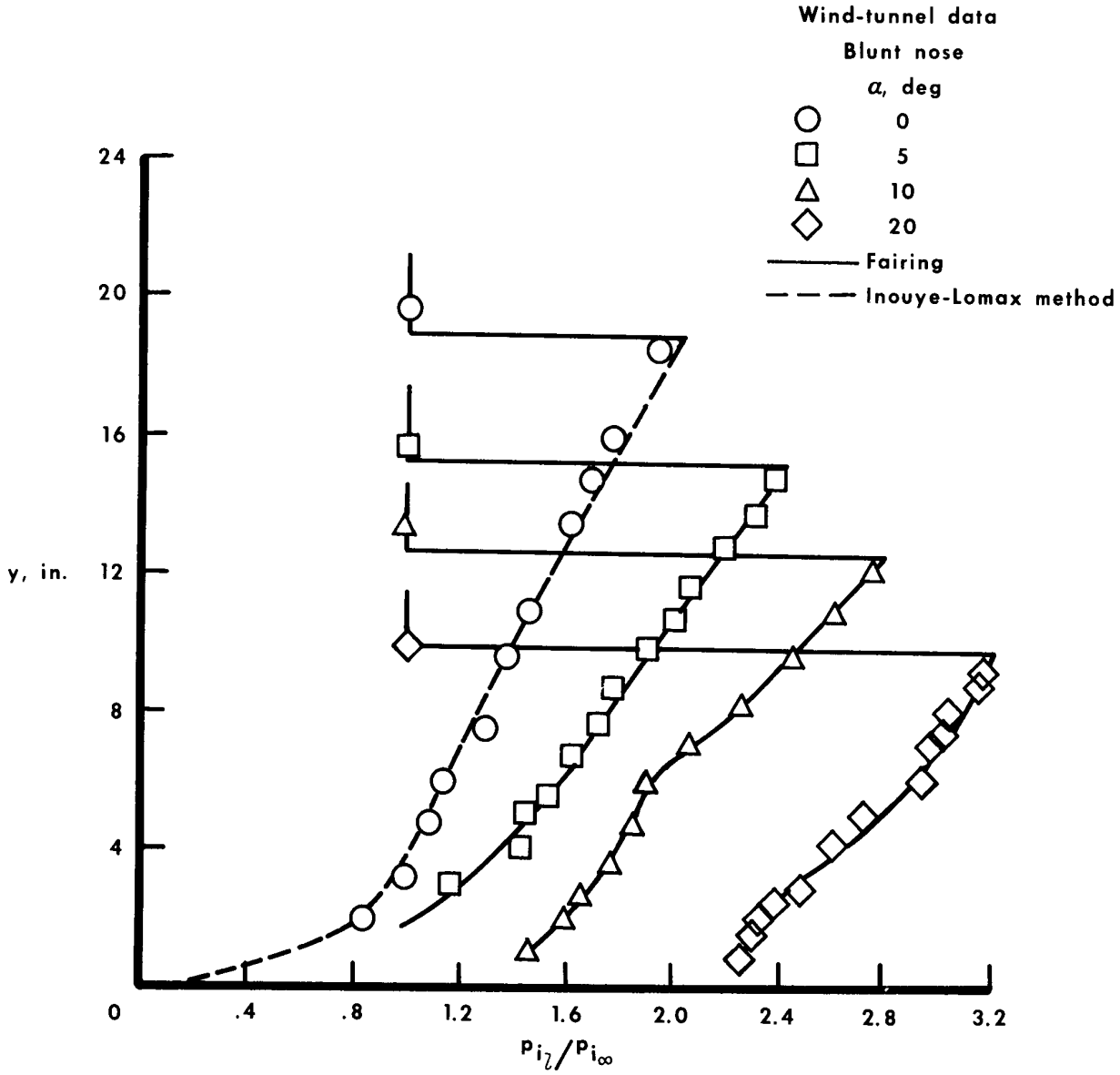

(d) x = 192 inches.

Figure 14.– Concluded.

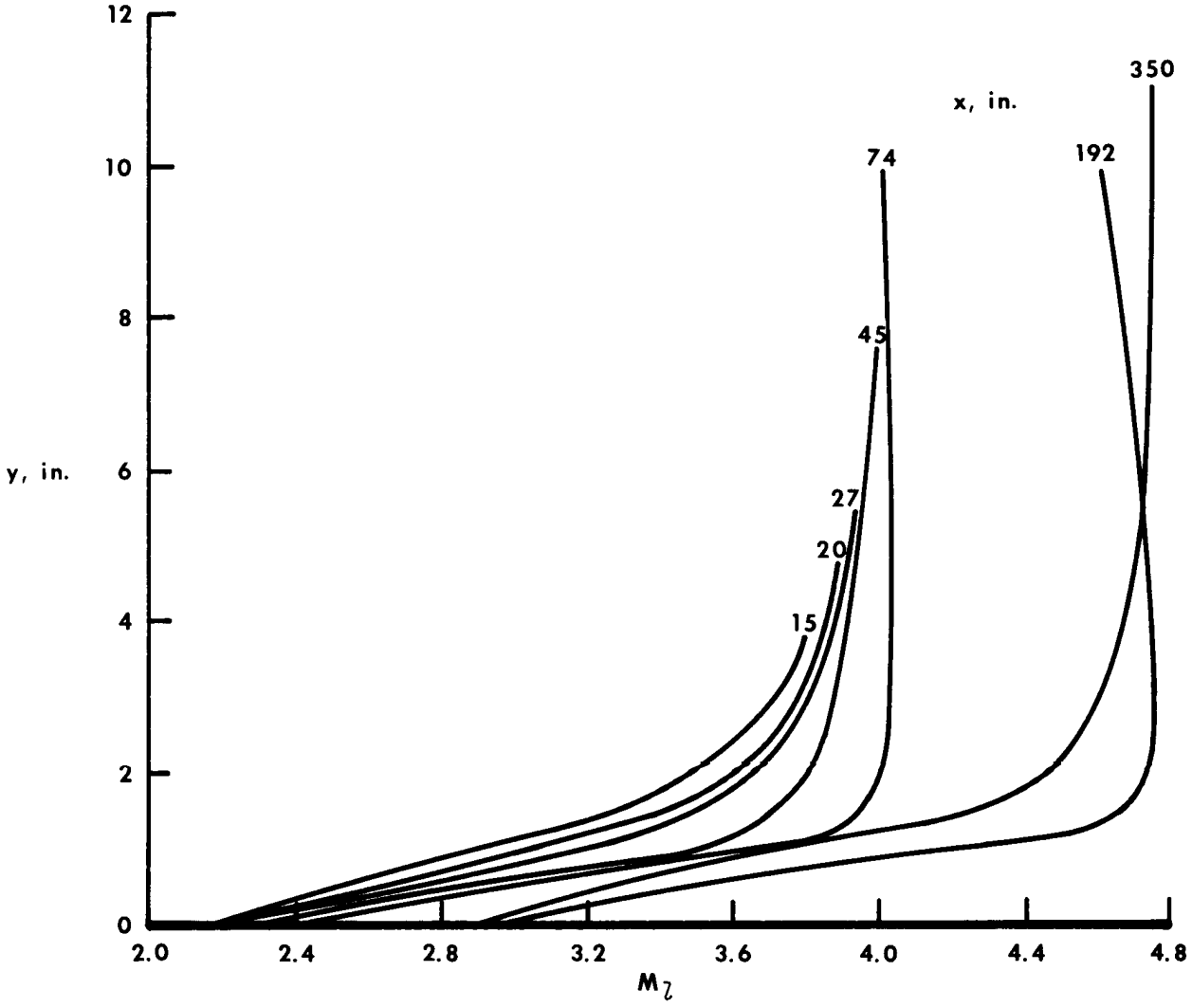

(a) $M_\infty = 4.7$.

Figure 15.– Theoretical variation of Mach number through the flow field at various longitudinal distances along the surface at $\alpha = 0^\circ$ as predicted by Inouye-Lomax solution.

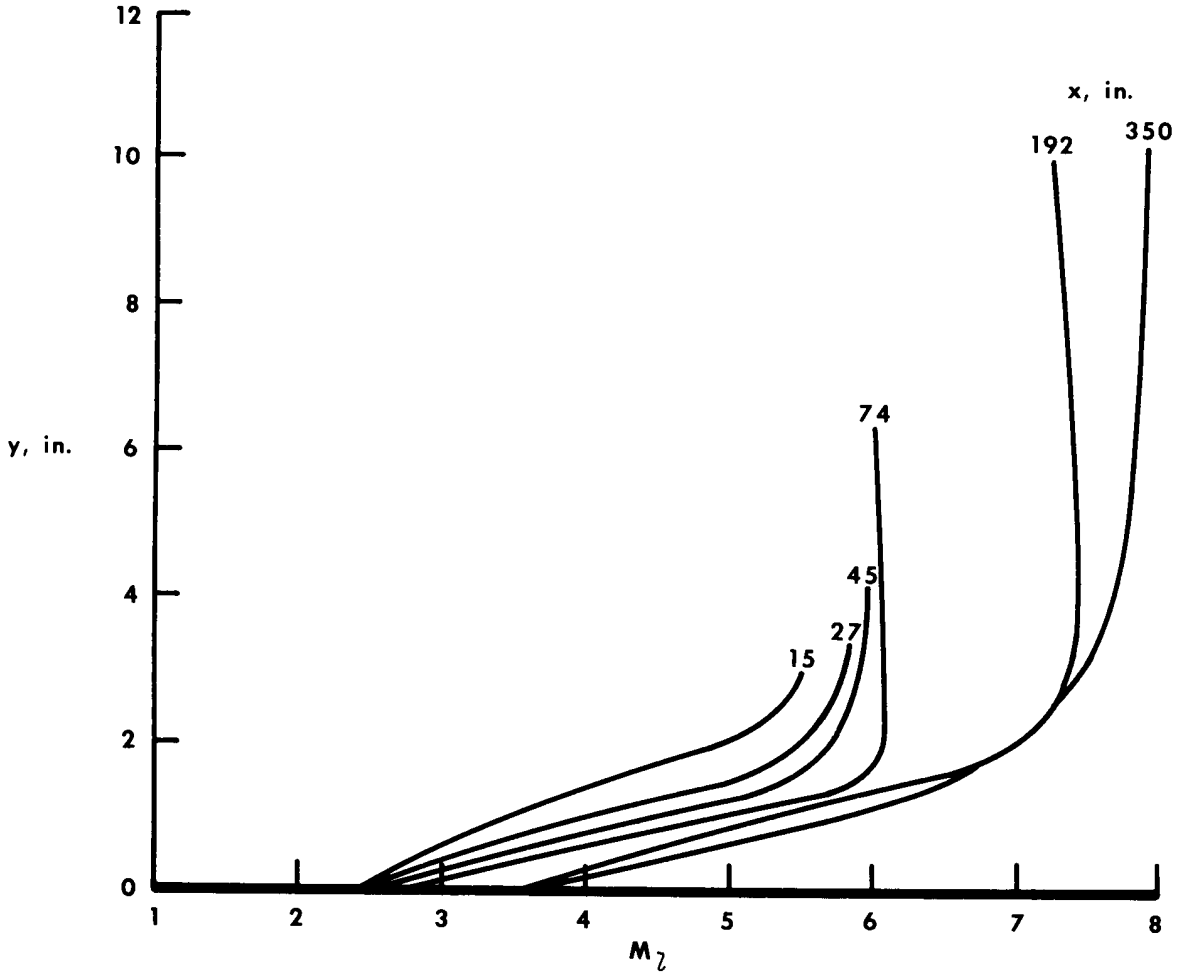

(b) $M_\infty = 8.0$.

Figure 15.– Concluded.

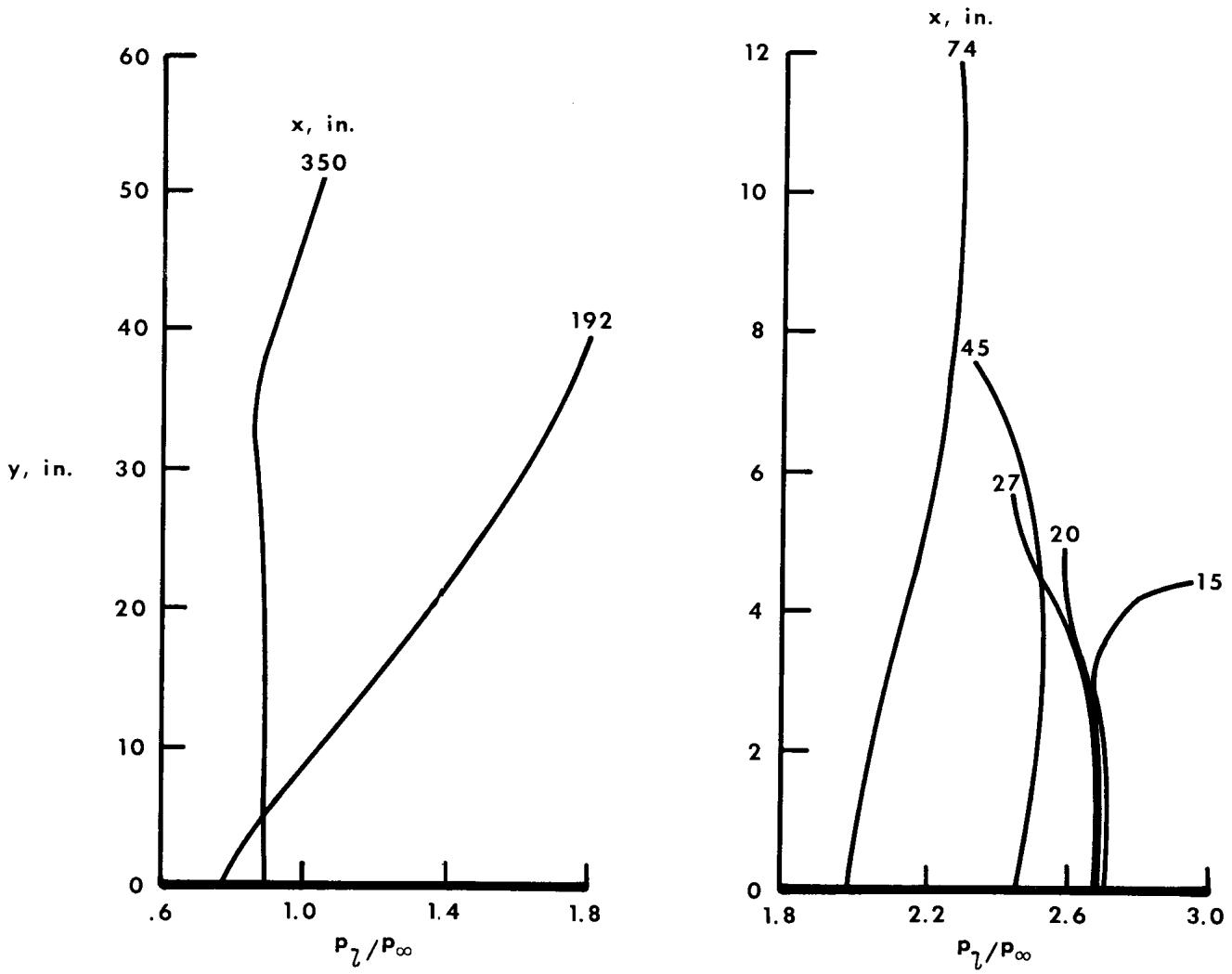

(a) $M_\infty = 4.7$.

Figure 16.– Theoretical variation of static pressure through the flow field at various longitudinal distances along the surface at $\alpha = 0^\circ$ as predicted by Inouye-Lomax solution.

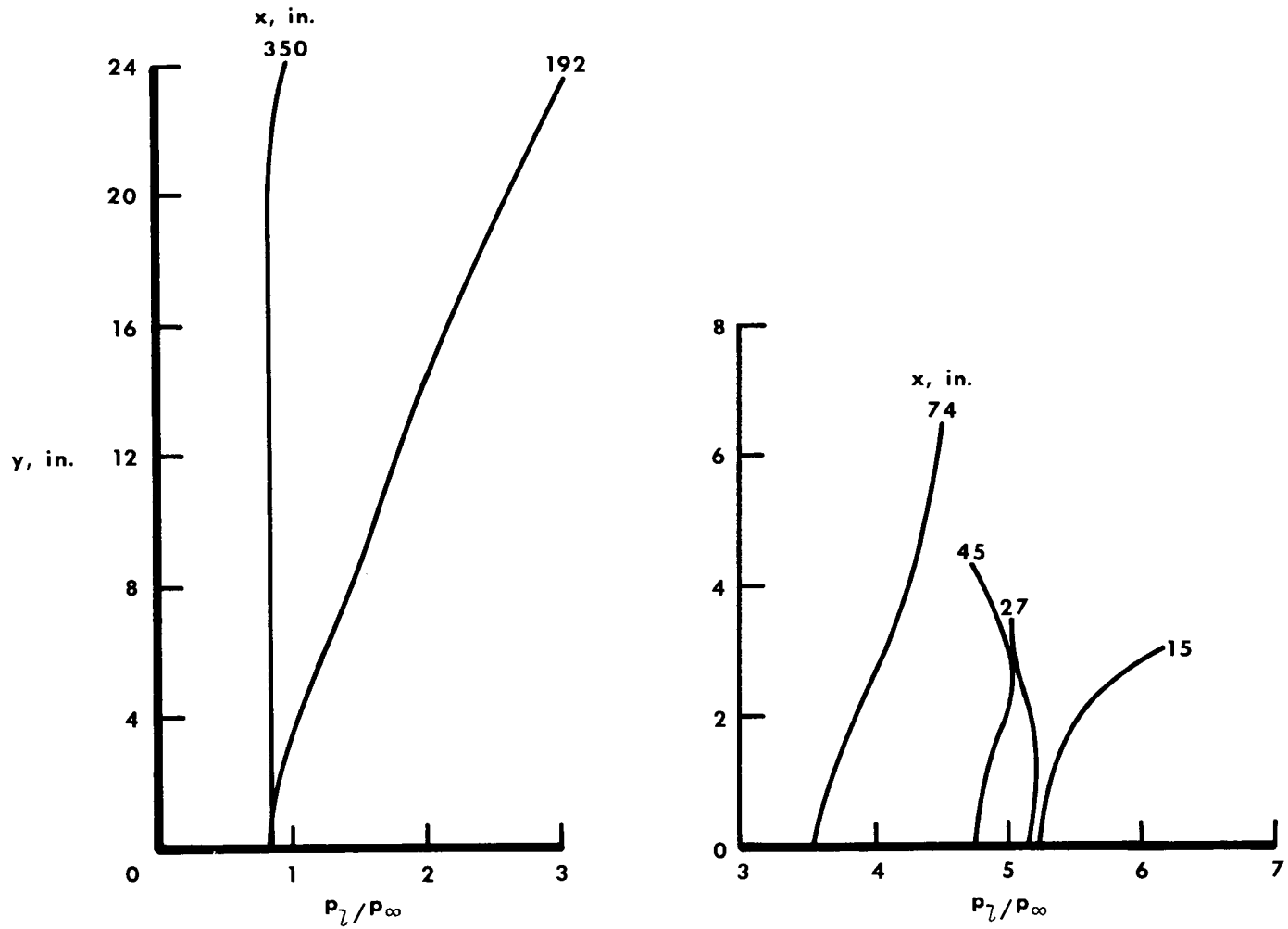

(b) $M_\infty = 8.0$.

Figure 16.– Concluded.

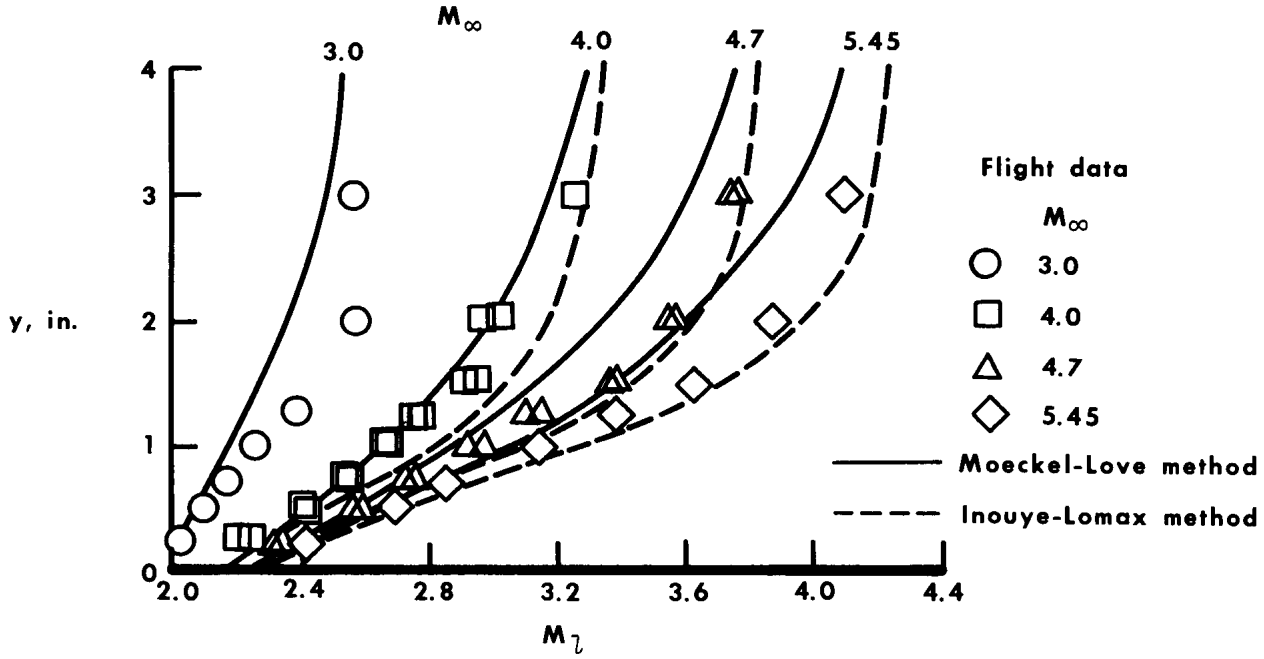

(a) x = 20 inches.

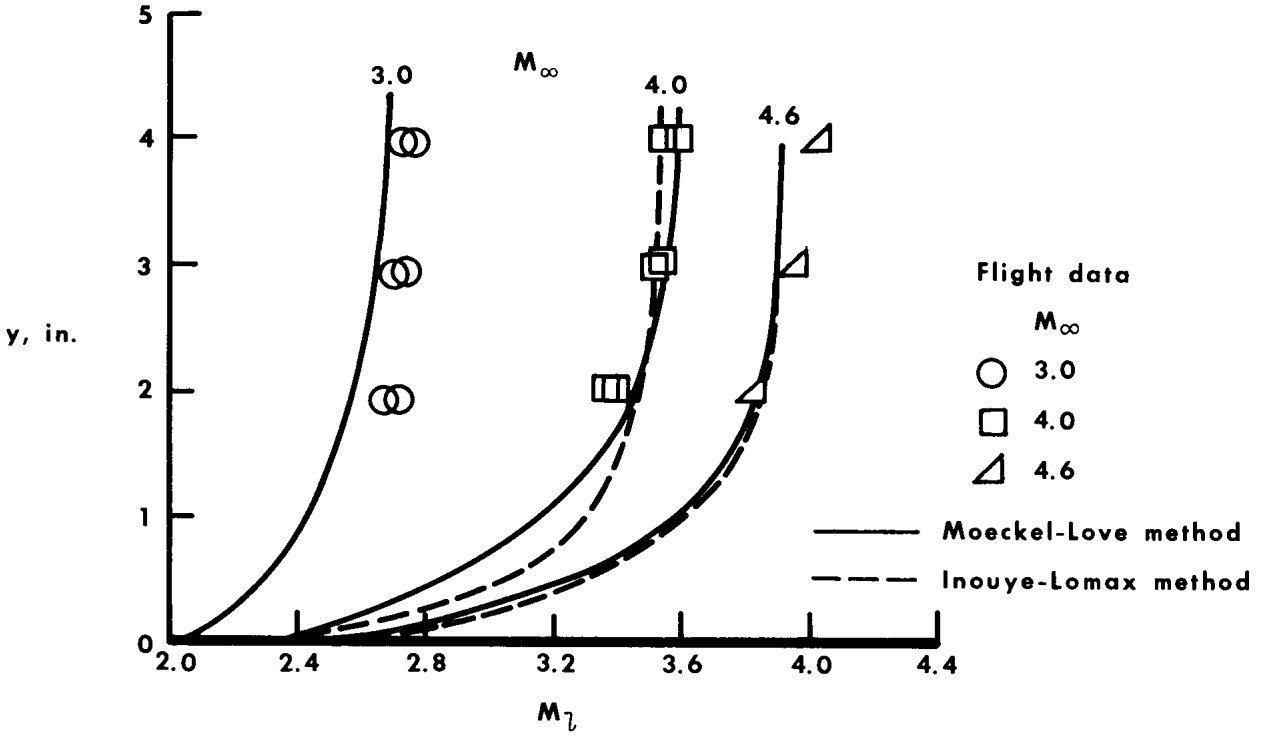

(b) x = 74 inches.

Figure 17.— Comparison of flight-derived local Mach number data with theoretical solutions at various free-stream Mach numbers. $\alpha = 0°$.

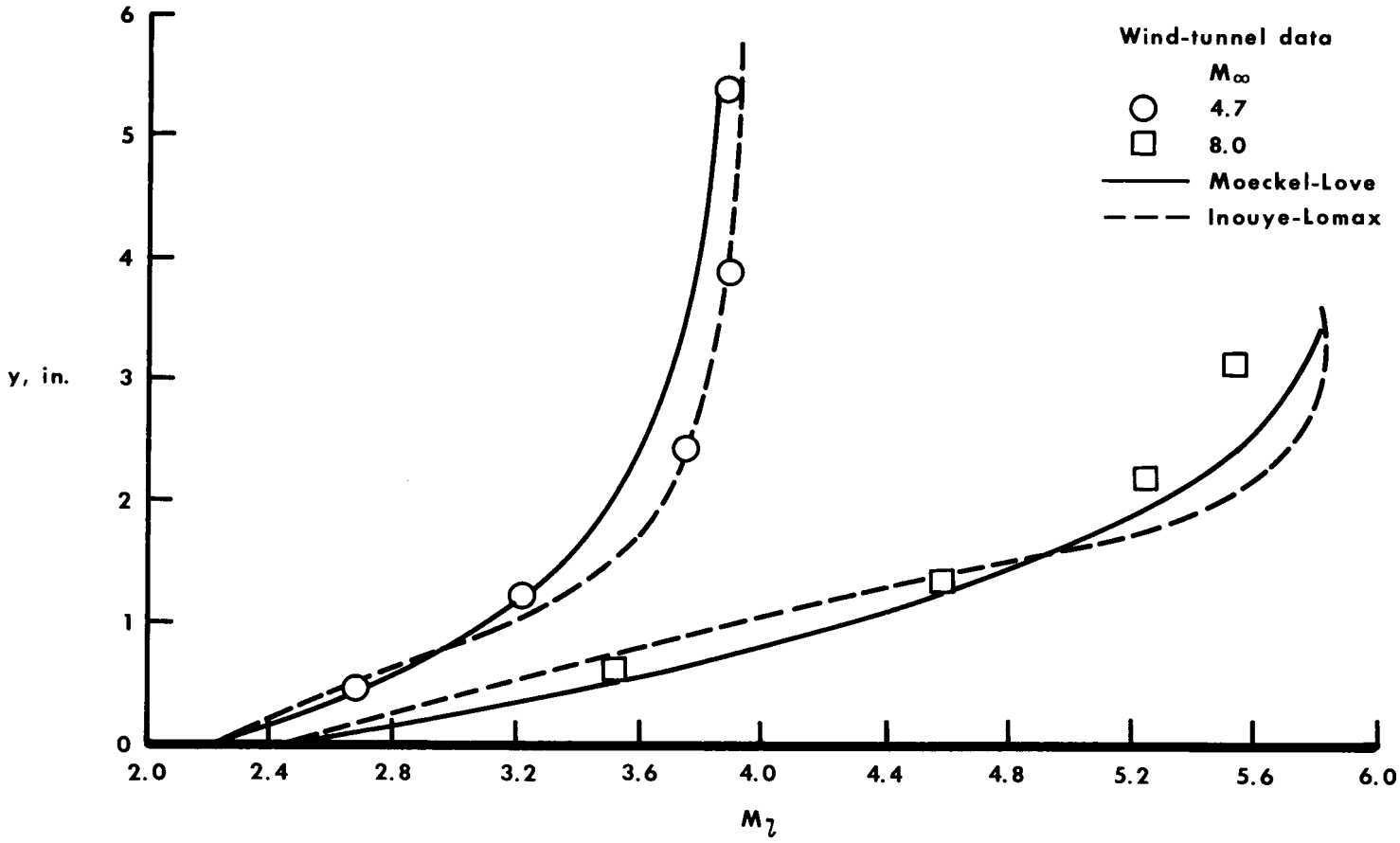

Figure 18.– Comparison of local Mach number derived from wind-tunnel data with results from theoretical solutions at two free-stream Mach numbers. x = 27 inch, $\alpha = 0°$.

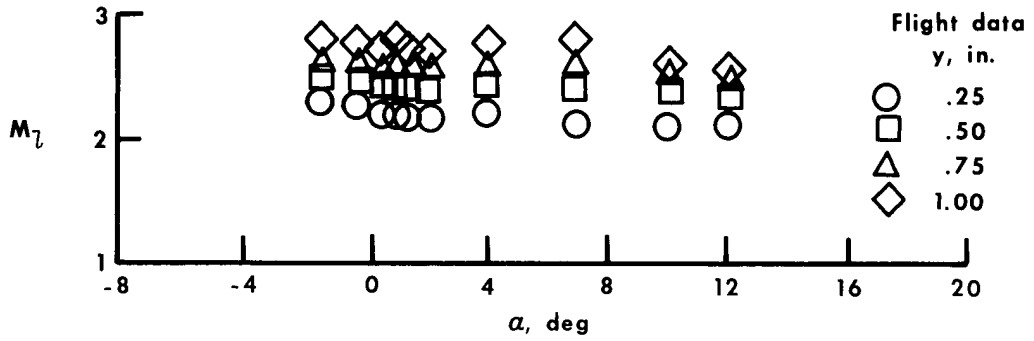

(a) $M_\infty = 4.0$.

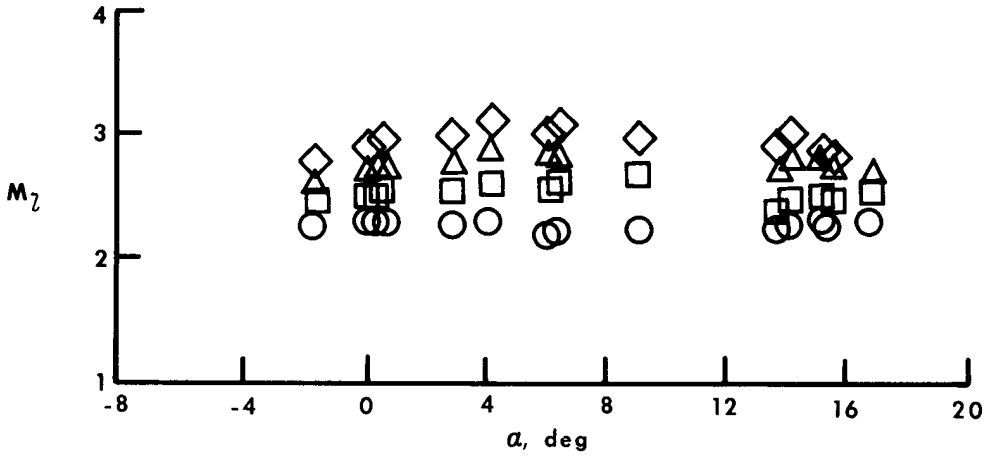

(b) $M_\infty = 4.7$.

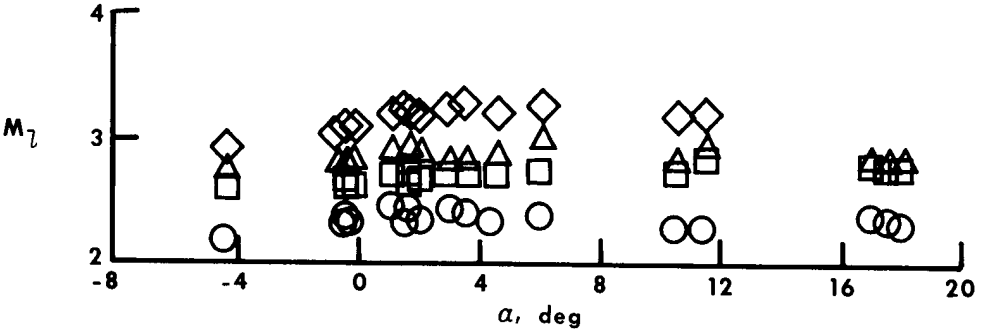

(c) $M_\infty = 5.4$.

Figure 19.– Effect of angle of attack on the local Mach number up to 1.0 inch from the surface. x = 20 inches.

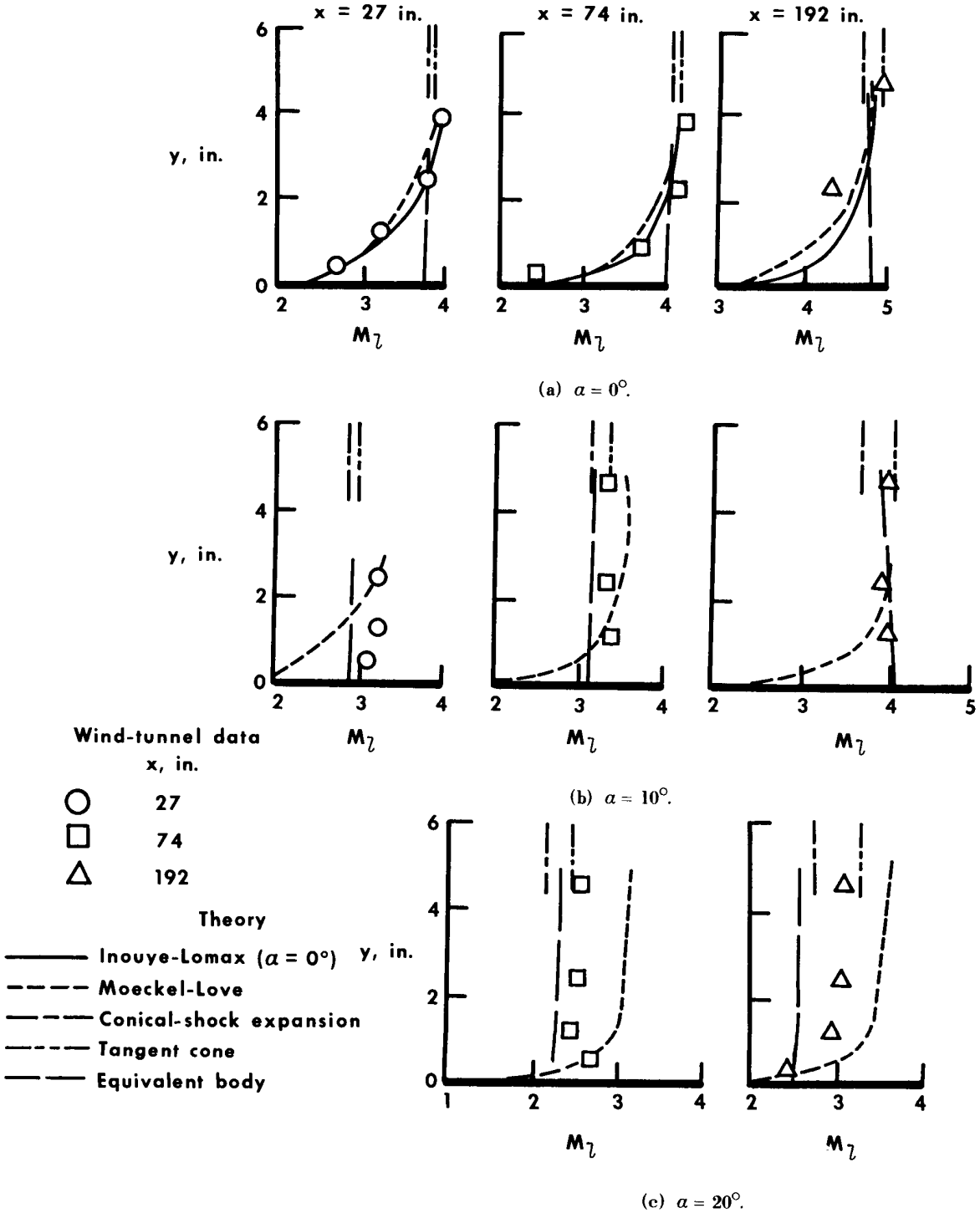

Figure 20.– Comparison with theory of local Mach number near the surface of the X-15 at various angles of attack and longitudinal distances. $M_\infty = 4.7$.

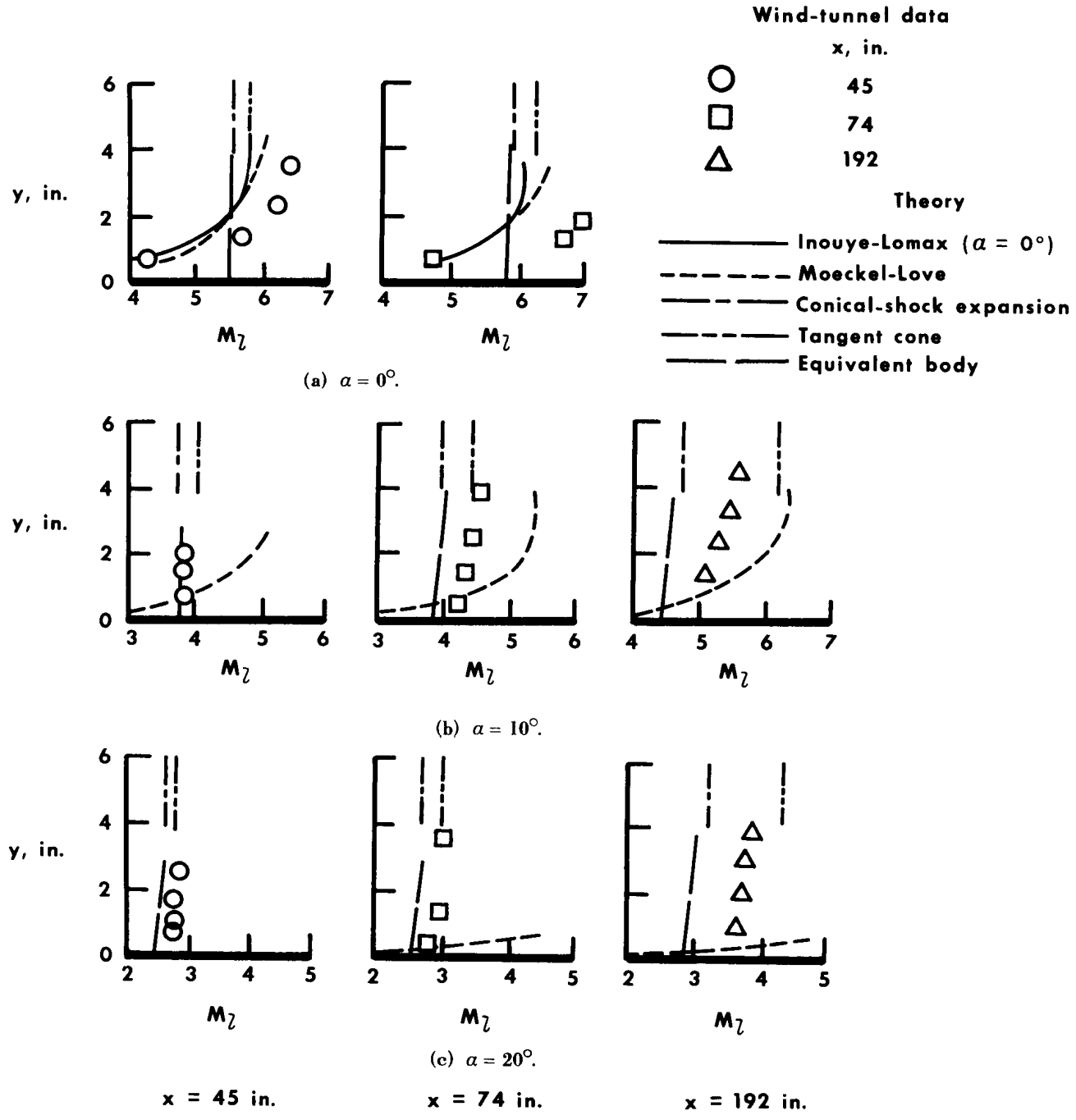

Figure 21.– Comparison with theory of local Mach number near the surface of the X-15 at various angles of attack and longitudinal distances. $M_\infty = 8.0$.